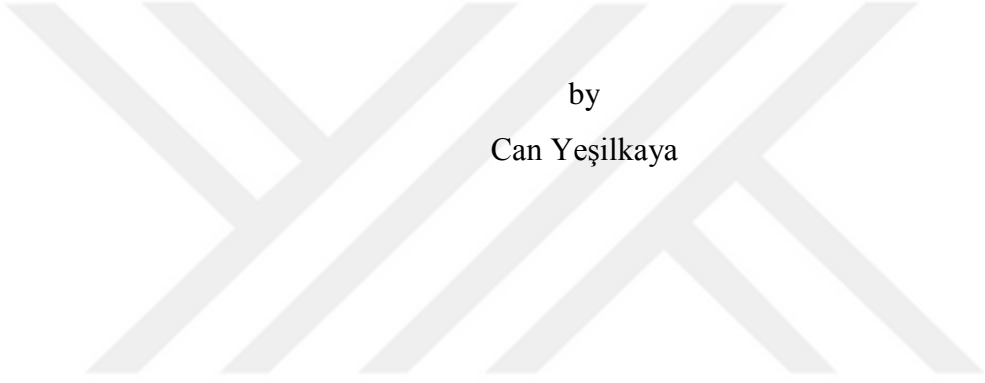


MODELING, ANALYSIS OF, AND EXPERIMENTATION ON AN ENERGY
HARVESTER DEVICE FOR TIRE PRESSURE MONITORING SYSTEMS



by
Can Yeşilkaya

Submitted to Graduate School of Natural and Applied Sciences
in Partial Fulfillment of the Requirements
for the Degree of Master of Science in
Mechanical Engineering

Yeditepe University

2015

MODELING, ANALYSIS OF, AND EXPERIMENTATION ON AN ENERGY
HARVESTER DEVICE FOR TIRE PRESSURE MONITORING SYSTEMS

APPROVED BY:

Assist. Prof. Dr. Namık CIBLAK
(Thesis Supervisor)



Prof. Dr. Ertugrul TACGIN



Assoc. Prof. Dr. Koray Kadir SAFAK



DATE OF APPROVAL: 10/09/2015

ACKNOWLEDGEMENTS

I would like to thank my advisor Mr. Cıblak firstly for his help for everything. I have the at most respect for his personality and knowledge. He has taught me a lot. I would like to thank my co-advisor Mr. Toplaoglu for his support. He has given a lot of ideas to me throughout this project. I have increased my knowledge and skills a great deal since I first started this project thanks to them.

I would like to thank my parents for their support when I was going through rough times and for all that they have provided for me. They cared for me for all my life and supported me. Thank you MOM, thank you DAD. I want to thank my girlfriend and fiancée Burcu Yavunc (Burcus) for her support and for believing in me and helping me throughout my master's program.

I would like to thank my friends Can Polat Cigay, Cagri Develi and Hasan Kalkan for listening when I constantly talked about the problems I went through. I would also like to thank Alp Can Akalin for his support and constantly playing PES with me and Cagri and for the beers they bought me. I consider them to be a part of my family.

ABSTRACT

MODELING, ANALYSIS OF, AND EXPERIMENTATION ON AN ENERGY HARVESTER DEVICE FOR TIRE PRESSURE MONITORING SYSTEMS

Tire pressure monitoring system (TPMS) is a system designed to monitor the air pressure inside vehicle tires and to provide an early warning system in case of low or high tire pressure. This technology is mandatory in many developed countries, as part of a global effort for increasing energy usage efficiency.

A standard TPMS device runs on batteries and thus there are issues regarding maintenance and disposal of these devices. Replacement of batteries increases the operational costs as well as resulting in a significant amount of pollution. A batteryless TPMS eliminates this problem. There is significant amount of research efforts on this topic and it is increasing.

In this thesis a novel, patent-pending design is modeled and simulated in a numerical software platform. The modeling includes collision modeling, dynamic equations of coupled electro-mechanical systems, and investigation of contact problems. For verification of the model a prototype is designed and constructed. Numerous experiments are conducted on the prototype.

The prototype is tested at low speeds and the numerical model is verified using the data gathered from the experiment and the numerical simulations. In both numerical and experimental cases, the maximum power output was obtained when the load resistance matched the generator internal resistance, a well-known fact. The numerical simulation is used to obtain power output of the system for vehicle speeds up to 150 km/h. It is seen that even at speeds as low as 20 km/h the harvester generated 2.2 mW of average power which is enough to energize a TPMS device.

ÖZET

PİLSİZ LASTİK BASINÇ İZLEME SİSTEMİ İÇİN TASARLANMIŞ ENERJİ ÜRETİM SİSTEMİNİN MODELLENMESİ, ANALİZİ VE DENEYSEL ANALİZİ

Lastik basınç izleme sistemleri (LBİS) tekerleklerdeki basıncı takip etmek ve düşük veya yüksek basınç durumlarında erken uyarı vermek için tasarlanmıştır. Bu teknolojinin kullanılması pek çok gelişmiş ülkede zorunlu hale gelmiştir.

Standart bir LBİS piller kullanılarak çalışmaktadır. Bu nedenle bu sistemlerin bakımı ve değiştirilmesi zor bir aşamadır. Pillerin değişme aşaması kayda değer bir anlamda çevre kirliliğine ve bakım maliyetini artmasına neden olmaktadır. Bu nedenle bu sistemleri pilleri devre dışı bırakacak bir enerji üretim sistemi tasarlanması gerekmektedir. Bu konu üzerine kayda değer miktarda çalışma bulunmaktadır ve bu çalışmaların sayısı gittikçe artmaktadır.

Bu tezde yeni ve patent başvurusu bulunan bir enerji üretim mekanizmasının modellenmesi ve bu modelin numerik bir yazılım kullanılarak çalıştırılması bulunmaktadır. Modelleme, çarpışma modellemesi, elektro-mekanik sistemlerin dinamik denklemlerinin modellenmesi ve temas problemlerinin araştırma ve çözülmesini içermektedir. Bu modellerin doğruluğunun onaylanması için enerji üretim sisteminin prototip tasarımı, üretimi yapılmış ve bu prototip üzerine deneyler yapılmıştır.

Enerji üretim sistemi düşük hızlarda denenmiştir ve toplanan veriler kullanılarak aynı testlerin sayısal benzetim sonuçları doğrulanmıştır. Enerji üretim sisteminin deneysel ve sayısal benzetim kullanılarak elde edilen maksimum güç jeneratörün iç direncine eş değer dirençte bulunmuştur. Sayısal benzetim 150 km/h ye kadar araç hızı için ortalama üretilen gücü hesaplamak için kullanılmıştır. Alınan sonuçlar aracın düşük hızlarda bile (20 km/h) 2.2 mW ortalama güç ürettiği bulunmuştur. Bu üretilen güç LBİS için yeterlilik göstermektedir.

TABLE OF CONTENTS

ACKNOWLEDGEMENTS.....	iii
ABSTRACT.....	iv
ÖZET	v
TABLE OF CONTENTS.....	vi
LIST OF FIGURES	viii
LIST OF TABLES.....	xii
LIST OF SYMBOLS AND ABBREVIATIONS	xiii
1. INTRODUCTION.....	1
1.1. TIRE PRESSURE MONITORING SYSTEM.....	3
1.1.1. Indirect Tire Pressure Monitoring System.....	3
1.1.2. Direct Tire Pressure Monitoring System	4
2. LITERATURE SURVEY	5
3. A NEW ENERGY HARVESTER CONCEPT.....	10
3.1. WORKING PRINCIPLE	12
3.2. CONICAL, HELICAL, AND TORSIONAL SPRINGS	12
3.2.1. Conical Compression Springs.....	12
3.2.2. Helical Springs.....	14
3.2.3. Torsional Springs.....	15
3.3. RATCHETS AND SIMILAR ELEMENTS	16
4. MODELING.....	18
4.1. STATICS OF THE ENERGY HARVESTER.....	18
4.2. TIRE DEFLECTION MODELING.....	23
4.3. CONICAL SPRING WITH EQUIVALENT MASS MODELING.....	28
4.3.1. Dynamics Of The Conical Spring.....	39
4.4. PULLEY MODEL	40
4.5. GENERATOR MODELING AND CHARACTERIZATION	42
4.5.1. Internal Resistance	45

4.5.2.	Motor Constant	45
4.5.3.	Damping Coefficient.....	48
4.5.4.	Inertia	50
4.5.5.	Inductance	53
4.6.	CONTACT/IMPACT PROBLEM MODELING	58
4.6.1.	Tip Of The Conical Spring And Base.....	58
4.6.2.	Rope Tightness	60
4.6.3.	Ratchet Engagement	61
5.	NUMERICAL SIMULATION	63
5.1.	CONTACT AND COLLISION PROBLEM SIMULATION	63
5.2.	COMPLETE POWER TRANSMISSION TO PULLEY	65
6.	EXPERIMENTAL DESIGN AND TESTING	67
6.1.	CAM DESIGN AND MECHANISM.....	67
6.2.	PROTOTYPE DESIGN GENERATION ONE.....	69
6.3.	PROTOTYPE DESIGN GENERATION TWO	72
6.4.	EXPERIMENTAL PROCEDURE	75
6.4.1.	Measuring The Voltage Generated.....	75
6.4.2.	Measuring Power Output.....	75
7.	RESULTS AND DISCUSSION.....	77
7.1.	OPEN CURCUIT EXPERIMENTS	77
7.2.	CLOSED CIRCUIT EXPERIMENTS.....	80
8.	CONCLUSION AND FUTURE WORK.....	83
	REFERENCES	84
	APPENDIX A: CONTACT AND COLLISION PROBLEM SIMULATION	88
	APPENDIX B: COMPLETE POWER TRANSMISSION TO PULLEY.....	96

LIST OF FIGURES

Figure 1.1. Contact patch for correct pressure, low pressure and high pressure (correct pressure contact patch is shown with dashed lines).....	2
Figure 2.1. An example of designs made by placing an inductor near the tire [15].....	6
Figure 2.2. Designs using centrifugal force. a) Lei Gu and Carol Livermore’s design [18]. b) F. Khameneifar et al.’s design [19] c) Manla et al.’s design [16, 17].....	7
Figure 2.3. A general schematic of a design made using a pendulum	8
Figure 2.4. Piezo-ceramic bender elements in tire surface for generating electricity [25-27]	8
Figure 3.1. The energy harvester design concept used in this study.	10
Figure 3.2. Main components of the designed energy harvester	11
Figure 3.3. Location of energy harvester inside the wheel	11
Figure 3.4. Load displacement graph of a general conical spring	13
Figure 3.5. Geometric dimensions of a conical spring [33].....	14
Figure 3.6. Sectional view of a ratchet and components [35].....	16
Figure 3.7. An example of a one-way bearing [36]	17
Figure 4.1. Assembly when the rope is connected to the pulley	18
Figure 4.2. The pulley and conical spring static equilibrium positions after the rope is connected to the conical spring.....	19
Figure 4.3. Free body diagrams of pulley and conical spring.....	20
Figure 4.4. Assembly with tire base	21
Figure 4.5. Simplified tire deflection model. The maximum deflection of the tire is r	23
Figure 4.6. Contact patch angle and reference angle θ	23

Figure 4.7. Radial deflection of tire vs. Angular position	24
Figure 4.8. The radial deflection, velocity and acceleration at 10 km/h.....	26
Figure 4.9. Maximum radial deflection velocity and acceleration vs. vehicle velocity	26
Figure 4.10. Conical spring with equivalent tip mass.....	28
Figure 4.11. Dimensions of a conical spring	30
Figure 4.12. Cone angle, pitch and inclination angle	31
Figure 4.13. Velocity profile of the conical spring.....	32
Figure 4.14. Mass Ratio vs. Cone Angle graph by variation in small radius	34
Figure 4.15. Solid Model of conical spring	35
Figure 4.16. Boundary conditon on the conical spring.....	36
Figure 4.17. Force applied to the tip of the conical spring	36
Figure 4.18. Results obtained by SolidWorks and ANSYS software.....	39
Figure 4.19. The pulley attached to the shaft.....	40
Figure 4.20. Pulley diagram with forces and moments	40
Figure 4.21. Free body diagram of pulley	41
Figure 4.22. Mabuchi RS-360SH DC motor	45
Figure 4.23. Rectangular part attached to shaft of motor	46
Figure 4.24. Voltage vs. angular velocity graph.....	47
Figure 4.25. Damping vs. angular velocity.....	49
Figure 4.26. Damping vs. angular velocity in 2-16 V range	49
Figure 4.27. Diagram of the inertia experiment system	50
Figure 4.28. Free-body diagrams (FBD) for motor inertia testing setup.....	51

Figure 4.29. The DC motor, and, a rope with weight attached.....	53
Figure 4.30. Circuit diagram of the experiment.....	54
Figure 4.31. Response of the motor internal circuit to a step input (Power Supply 1).....	56
Figure 4.32. Response of the motor internal circuit to a step input (Power Supply 2).....	57
Figure 4.33. Response of the motor internal circuit to a step input using 9V battery.	57
Figure 4.34. Positions of tire and spring as measured from the undeflected tire position...59	
Figure 4.35. Driving and driven angular velocities	61
Figure 5.1. Flowchart of Contact and Collision Problem Simulation	64
Figure 5.2. Flowchart of complete power transmission to pulley simulation case.....	66
Figure 6.1. Basic sketch of the designed cam.....	67
Figure 6.2. Cam obtained by placing a bar inside a circular part	68
Figure 6.3. Structure where the DC motor and the Cam is placed	68
Figure 6.4. Components of the main structure.....	69
Figure 6.5. Prototype generation One	69
Figure 6.6. Components of the prototype generation one.....	70
Figure 6.7. Prototype placed on the main structure of the cam	71
Figure 6.8. Prototype test results	72
Figure 6.9. Helical coupling used to relieve the unwanted loads on the bearing	72
Figure 6.10. The prototype with the helical coupling and new torsional spring.	73
Figure 6.11. Deflection and force data obtained from universal testing machine	74
Figure 6.12. Prototype test results	75
Figure 6.13. Diagram of the circuit in order to measure power output over the resistor.....	76

Figure 7.1. Voltage generated by applying 3V to the main DC motor.....77

Figure 7.2. Numerical simulation results for tire period of 0.89 seconds.....78

Figure 7.3. Voltage generated by applying 4V to the main DC motor.....79

Figure 7.4. Numerical simulation results for tire period of 0.41 seconds.....79

Figure 7.5. Maximum power obtained for experiment and numerical simulation81

Figure 7.6. Average power simulation results vs. vehicle speed.82



LIST OF TABLES

Table 4.1. Dimensions of the solid model conical spring.....	35
Table 4.2. Material properties of AISI 1020 cold rolled steel	36
Table 4.3. The values of applied forces	37
Table 4.4. Applied forces and obtained tip displacements	37
Table 4.5. Results for displacement obtained by using ANSYS	38
Table 4.6. Voltage and angular velocity data	47
Table 4.7. Calculated angular velocity and damping data.....	48
Table 4.8. Initial height, weight and shaft radius values used	53
Table 6.1. Helical spring properties used in the prototype	70
Table 6.2. The properties of the helical spring used in place of the torsional spring.	73
Table 7.1. Summary of the results obtained from applying 3 V to the main DC motor.....	78
Table 7.2. Summary of the results obtained from applying 4 V to the main DC motor.....	80

LIST OF SYMBOLS AND ABBREVIATIONS

β	Contact patch angle
ζ	Damping ratio of the conical spring, damping ratio of pulley assembly
θ_{ps}	Static position of pulley
ρ	Density of the material of spring
ψ	The helix angle of the conical spring
ω	Tire angular speed
ω_d	Damped natural frequency of the conical spring, damped natural frequency of pulley assembly
ω_n	Natural frequency of the conical spring, natural frequency of pulley assembly
A	The cross sectional area of the conical spring
b	Viscous damping of conical spring, viscous damping of pulley
d	Wire thickness of the spring
D	Mean coil diameter of helical spring
D_{max}	Maximum mean coil diameter
D_{min}	Minimum mean coil diameter
E	Young's modulus of the spring material
G	Shear modulus of the spring material
H	Distance between tip of conical spring and center of pulley
h_b	Thickness of base of assembly
h_p	Distance of pulley center from base of assembly
I_p	Pulley inertia
I_s	Pulley shaft inertia
J	Inertia of the DC motor
k	DC motor constant, helical spring stiffness
k_c	Conical spring stiffness
k_t	Torsional spring angular stiffness
L	Inductance

L_f	Free length of spring
L_r	Rope length
m	Total mass of conical spring
m_{eq}	Equivalent mass of conical spring
N	Number of active coils
N_b	Number of body turns of torsional spring
P	Pitch of conical spring
p_{cs}	Static position of spring
r	Maximum deflection of tire
R	Radius of tire
R_{load}	Load resistance
R_m	Coil resistance
r_p	Pulley radius
V	Vehicle speed
DAQ	Data acquisition
$dTPMS$	Direct tire pressure monitoring system
$iTPMS$	Indirect tire pressure monitoring system
$TPMS$	Tire pressure monitoring system

1. INTRODUCTION

Tire pressure monitoring system (TPMS) is a system designed to monitor the air pressure inside tires of vehicles and provide an early warning system in case of low or high tire pressure. This technology is mandatory in many developed countries, as part of the global effort for increasing energy usage efficiency. There are two types of TPMS systems these are indirect TPMS (iTPMS) and direct TPMS (dTPMS). iTPMS systems do not use pressure sensors, they estimate the tire pressure using the angular velocity of the tire. dTPMS systems use pressure sensors placed inside the tire and they usually require a battery as a power supply.

In this thesis a novel, patent-pending design is proposed to be modeled and implemented in a numerical software platform. The modeling includes collision modeling, dynamic equations of coupled electro-mechanical systems, and investigation of contact problems. For verification of the model a prototype is designed and constructed. Numerous experiments are conducted on the prototype.

In vehicles, pneumatic tire pressures are very important since the contact between the ground and the vehicle is made using tires. The area of the contact is called the contact patch. For the contact patch to form properly, tire specific operating pressures must follow the directions provided by the tire manufacturers. If the pressure is different than the pressure value provided by the manufacturer the contact patch between the ground and the tire changes, Figure 1.1. Fuel efficiency is directly dependent on tire pressures. For every 3.3 psi (0.23 bar) pressure drop the fuel efficiency is reduced by 1 percent [1].

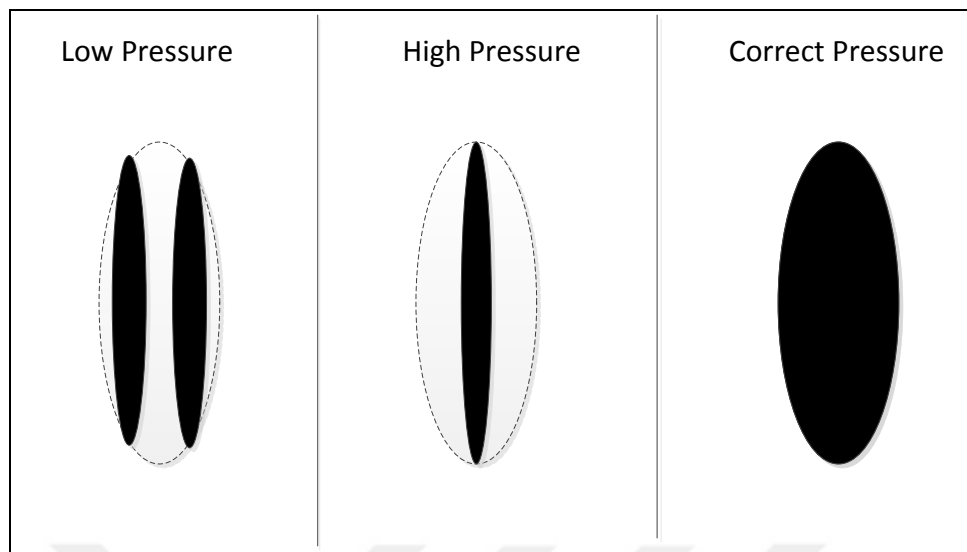


Figure 1.1. Contact patch for correct pressure, low pressure and high pressure (correct pressure contact patch is shown with dashed lines)

Tire failures are known to be caused by several factors including under inflation and overloading. An estimated 414 fatalities and 10275 non-fatal injuries result annually from tire related problems (e.g., flat tires, blowouts). Under inflation is involved in 20% of flat tire/blowout cases that result in a crash [2]. For example, in 1990s incidents of unexpectedly large number of tire failures involving Firestone, a US based tire manufacturer, tires and consequent recalls, led NHTSA (National Highway Traffic Safety Administration, US) to undertake an investigation of the causes underlying the failures. The technical investigation was undertaken by Ford Company, the main customer of the tires, which determined “under-inflation” as one of the main factors.

These incidents also pushed the United States Congress to legislate in 2000 the TREAD Act that mandated the use of a suitable Tire Pressure Monitoring System (TPMS) technology in all motor vehicles under 4.5 tons in order to help alert drivers of under inflation events. This act was to apply to all such vehicles that were to be manufactured after September 1, 2007, [3].

Similarly, in the European Union, all new M1 class (8 or less seats) passenger car models are required to be equipped with a TPMS as of November 1, 2012. Since November 1, 2014, all new passenger cars sold in the European Union must be equipped with TPMS.

1.1. TIRE PRESSURE MONITORING SYSTEM

TPMS are electrical or electro-mechanical systems designed to monitor the pressure inside pneumatic tires. The aim of TPMS systems is to avoid traffic accidents caused by tire failures and to increase the fuel efficiency by decreasing the energy losses due to under or over inflated tires. There are two types of TPMS:

- i. Indirect TPMS (iTPMS), and
- ii. Direct TPMS (dTPMS).

In what follows, these systems are explained in more detail.

1.1.1. Indirect Tire Pressure Monitoring System

iTPMS do not use physical pressure sensors, instead they estimate air pressure indirectly by monitoring individual wheel rotational speeds and other signals available from outside of the tire, [4].

First generation iTPMS are based on the principle that under inflated tires have slightly smaller diameters than a correctly inflated one. Therefore, an underinflated tire would rotate faster than a normal one for a given vehicle speed. Hence, only measuring the tire rotation speed, it is, in principle, possible to estimate the effective tire diameter and, in turn, the tire pressure.

Second generation iTPMS detect under inflation using vibration data of the tire assembly. It has been shown that some of the frequencies in the spectrum are sensitive to the tire pressure. Therefore, a spectrum analysis, done by signal processing software, enables monitoring of such signature frequencies.

One of advantages of the iTPMS is that they do not require access into the tire for direct measurement of the pressure. Therefore, no change is required in tire assembly. Also, since they are powered by the car battery, they do not require additional batteries, which make them an environmentally friendly choice.

The drawback in iTPMS is that since these devices cannot measure absolute pressure of the tire they are relative by nature. They need to be reset by the driver when the pressure in the tire is known to be correct. iTPMS devices do not show the specific tire in which the pressure is low. Further, if a tire size not recommended by the manufacturer is used, the estimation errors may increase.

1.1.2. Direct Tire Pressure Monitoring System

dTPMS, measures the pressures of the tires directly by using external or internal sensors. These sensors require an energy source to work. Some sensors use electromagnetic induction as wireless power systems, other types usually use batteries. Current research focuses on another alternative, namely systems that generate its own power using the motion of the tire.

Most dTPMS are mounted on the inside of the rim and use fixed batteries which are not replaceable. Typically dTPMS uses around 250 μ w [5] A battery replacement means that the whole sensor will have to be replaced. The replacement is possible only by dismounting the tire. Therefore, the lifetime of the battery becomes a crucial parameter and this process has a considerable pollution effect on the environment. Further, since these sensors are subjected to very harsh environmental conditions inside the tire, the endurance and reliability of particular designs become critical issues for practical applications.

This report contains a literature survey on energy harvester designs for TPMS in Section 2. An energy harvester mechanism proposed by Ciblak and Topaloglu is explained in Section 3. The proposed harvester is modeled in Section 4 and using these models numerical simulation algorithms are written, these algorithms are explained in Section 5. A prototype is designed and constructed of the proposed mechanism, this is explained in Section 6. Voltage output data of the mechanism in open circuit and power output data of the mechanism in closed circuit mode are gathered, and presented and discussed in Section 7.

2. LITERATURE SURVEY

Energy harvesters have been around for centuries for high power applications such as windmills and water mills. These types of system generate a significantly large amount of power and are large in size. Other than these energy types micro fuel cells [6] and micro turbine [7] generators are investigated. These systems are capable of providing large power outputs, but both require refueling. However, for low power applications such as a sensor power input, smaller energy harvesters are used which use the ambient power sources such as light, thermal energy and kinetic energy (mostly in form of vibration).

Solar energy cells can be used to harvest power from light sources. These type of applications provide high power density in direct lighting but have very limited output under dim lighting conditions. Thus this makes them unsuitable for embedded applications where the lighting condition is far from ideal condition for the solar cells.

Thermal energy can be converted to electrical energy using Seebeck effect. The early applications of these types of harvesters generated a few nW of power output [8].

Kinetic energy from vibration is generally harvested by using electromagnetic, piezoelectric or electrostatic transducers. The most basic form of harvesting energy using piezoelectric material is by using a cantilever beam covered with piezoelectric material [9]. Electromagnetic generators are used for vibration energy harvesting by, placing magnets on a cantilever beam and by placing a coil in the moving magnetic field [10].

The topic of batteryless TPMS is an ongoing research. There are numerous journal papers and patents related to this subject which are written over the last few years.

There are designs utilizing an inductive element near the tire [11-14]. The aim in this method is to place an inductor connected to the battery of the vehicle and to provide power input to the TPMS using inductance.

Designs involving inductive elements may be viable in the future if the car manufacturers integrate an antenna system which is powered from the car battery, which would be placed near tires. This method is not feasible as an aftermarket solution today since this antenna cannot be mounted to the vehicle by the driver and the system itself is prone to theft since it is mounted outside the vehicle.

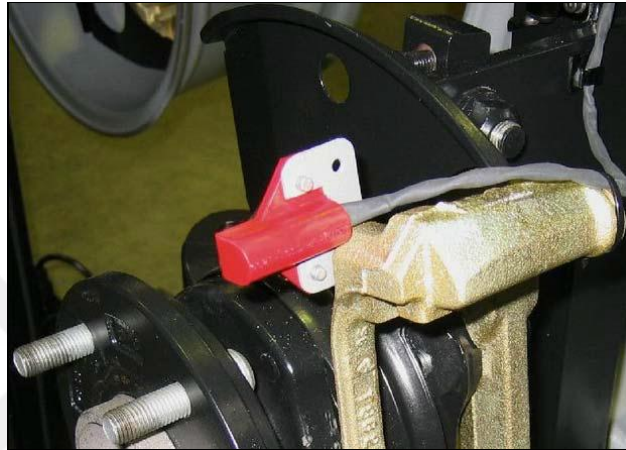


Figure 2.1. An example of designs made by placing an inductor near the tire [15]

There are designs that take advantage of the centrifugal force [16-19]. The centrifugal force increases as the vehicle velocity increases. Some of these are explained below.

In Figure 2.2. a) Lei Gu and Carol Livermore's design is shown [18]. They have designed two beams, one containing a tip mass and the other beam made out of piezoelectric material. Due to gravity the beam with the tip mass impacts on the piezoelectric beam. However the power generated using this method is in micro watt level thus it is not suitable for use.

In Figure 2.2. b) F. Khameneifar et al.'s design is shown [19]. A beam made out of piezoelectric material has a tip mass and due to acceleration the beam bends and thus a power output is obtained.

In Figure 2.2. c) Manla et al.'s designs are shown [16, 17]. In this design a ball is put inside a box with walls of piezoelectric material. As the tire rotates the ball impacts on the

piezoelectric plates and a power output is generated. This mechanism is not suitable for use due to its complicated and heavy structure.

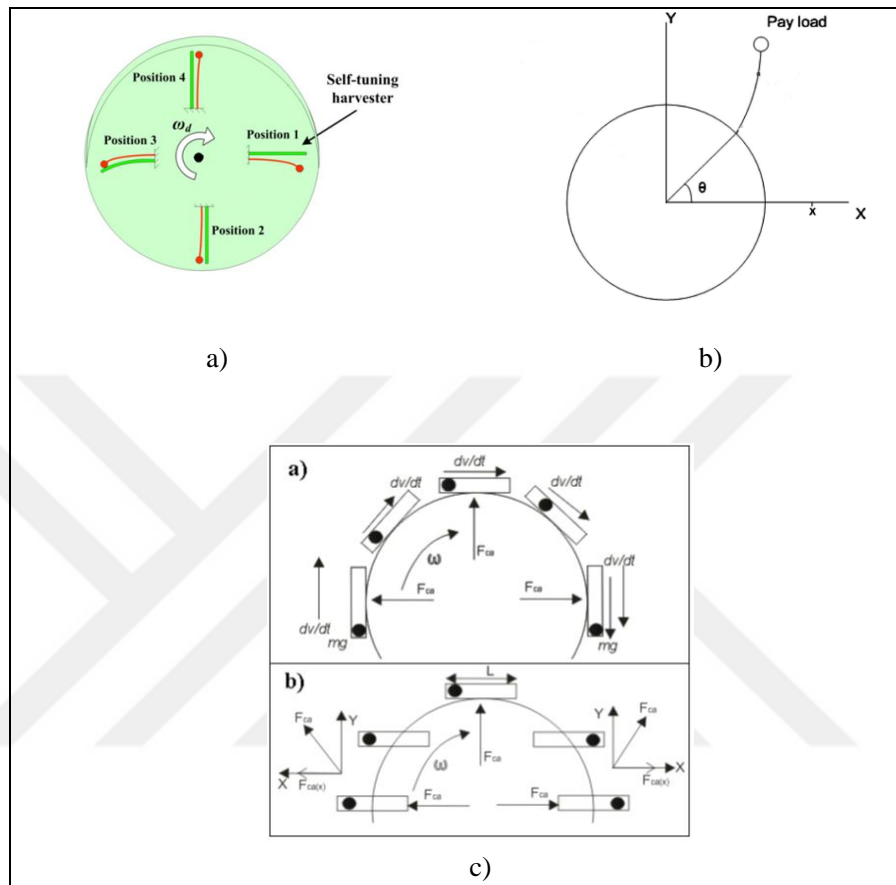


Figure 2.2. Designs using centrifugal force. a) Lei Gu and Carol Livermore's design [18].

b) F. Khameneifar et al.'s design [19] c) Manla et al.'s design [16, 17]

There are designs made by using pendulum type mechanisms [20-24]. A dynamo cannot be used in these applications due to it being in need of a stationary component. In these types of designs a pendulum is placed somewhere other than the center of the tire and due to its mass does not fully rotate with the tire. This is used as a stationary point for the dynamo. This concept is shown in Figure 2.3.

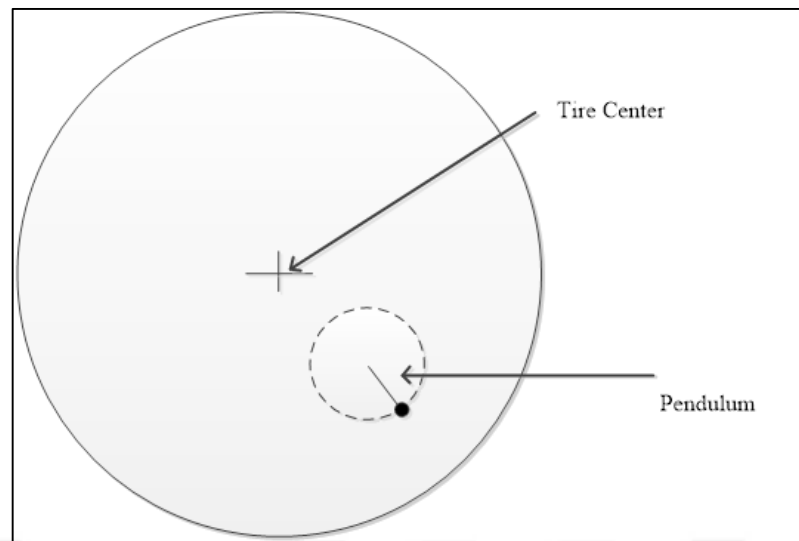


Figure 2.3. A general schematic of a design made using a pendulum

A widely seen problem with these types of designs is that at high speeds the centrifugal force becomes more dominant and the pendulum starts to rotate with the tire. As the vehicle moves the pendulum can have a chaotic motion and can cause unwanted dynamical effects to the vehicle.

There are designs that take advantage of tire deformation and contact patch formation [25-30]. A point on the tire is subjected to deformation periodically due to contact patch forming. A good example for this type of design can be given using Makki's work [25-27] shown in Figure 2.4. The method is to place highly flexible piezo-ceramic bender elements to the tire surface.



Figure 2.4. Piezo-ceramic bender elements in tire surface for generating electricity [25-27]

Although the power output of this system is enough for a TPMS device it is hard to mount this inside the tire without any problems and it is not practical to dismount and mount the system again when changing tires.



3. A NEW ENERGY HARVESTER CONCEPT

In this section, the energy harvester mechanism used in this study is presented. This mechanism is based on an original concept proposed by Ciblak and Topaloglu (Figure 3.1.) in order to suit the power supply need of the TPMS and to address the pollution and maintenance problems mentioned in section 1.1.2 [31].

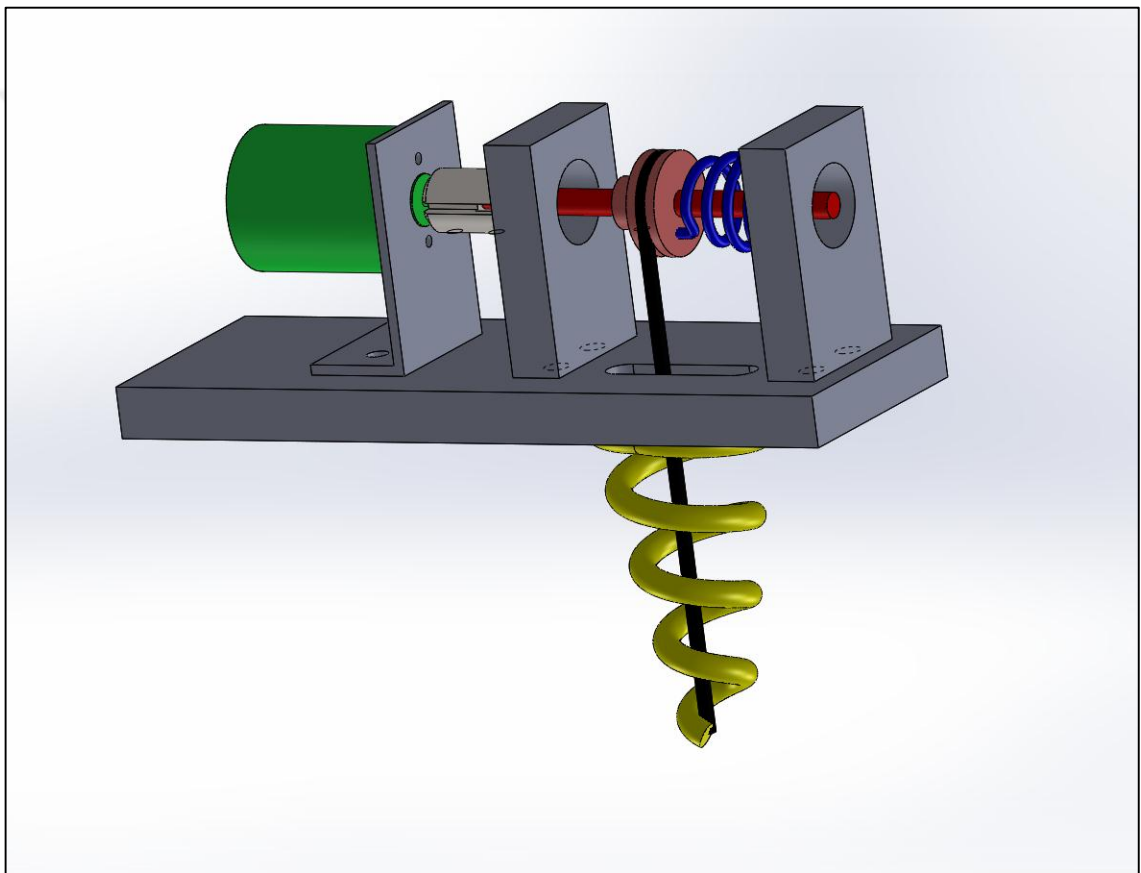


Figure 3.1. The energy harvester design concept used in this study.

The main components of this harvester are shown in Figure 3.2. from the side view of the design.

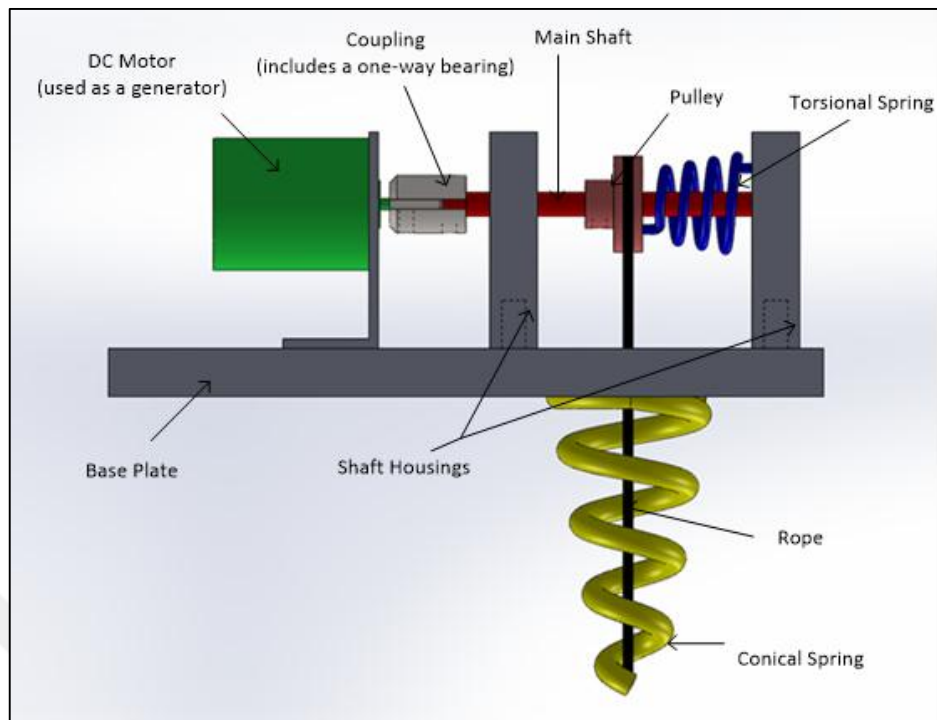


Figure 3.2. Main components of the designed energy harvester

The conical spring is used in order to minimize the solid height of the spring, which then protects the whole mechanism in case of flat tire. One-way bearing is used to transfer motion from the shaft of the pulley to the generator only in a one direction, removing the load from the generator when the pulley runs in the other direction. In actual design, the harvester is to be mounted on the rim inside the tire, as shown in Figure 3.3.

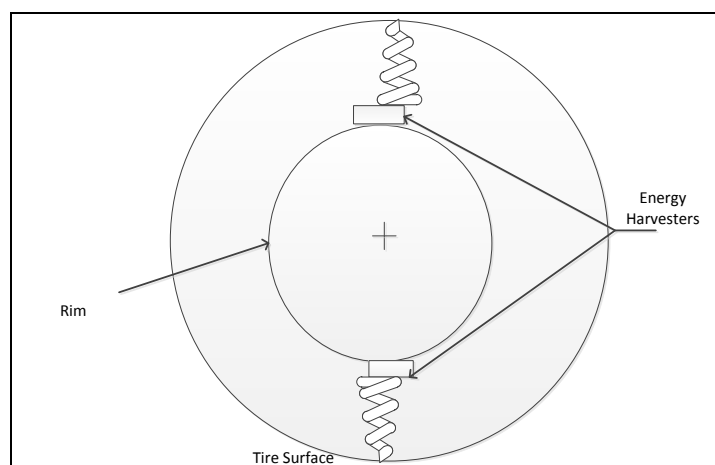


Figure 3.3. Location of energy harvester inside the wheel

3.1. WORKING PRINCIPLE

When the tire deflects the conical spring compresses and the rope gets loose for a moment. The torsional spring located next to the pulley then winds up the rope to keep it tight constantly. During this interval there is no motion transferred to the generator, due to the use of the one way bearing.

When the tire deflection ends, the conical spring moves with the tire and the rope is unwound from the pulley. Here the one way bearing engages and the motion is transmitted to the generator and electricity is generated. If the generator is connected to a circuit a current is obtained. Otherwise if the generator is not attached to a circuit, an open circuit electrical potential difference develops between the terminals.

In order for the TPMS to work efficiently, the rope should remain tight, and, the contact between the tire and the conical spring should be sustained at all times. These conditions require careful design of system components. In subsequent sections, design of these components are presented in detail.

3.2. CONICAL, HELICAL, AND TORSIONAL SPRINGS

In this section, the springs used in the concept model and the prototype are studied. Although the concept calls for a conical spring, the prototype uses a helical one due to its simplicity and availability. This is justified since the main reason in using a conical spring is to prevent mechanism failure in case of flat tire.

3.2.1. Conical Compression Springs

Conical springs have nonlinear stiffness over its full range. The load displacement graph of a general conical spring is shown in Figure 3.4.

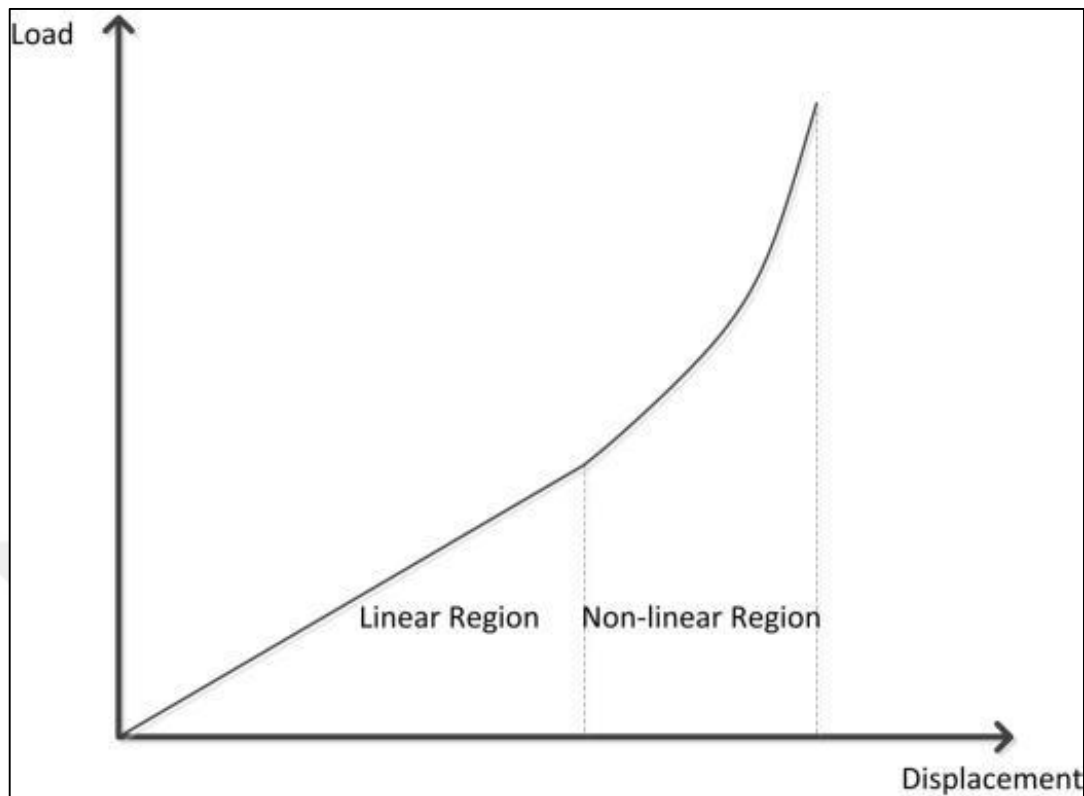


Figure 3.4. Load displacement graph of a general conical spring

For the linear region, the force-displacement relationship can be expressed using Hooke's law, as given below.

$$F = k_c z \quad (3.1)$$

where z is the displacement from load-free condition and F is the corresponding force. For the nonlinear region the force displacement relationship is given in [32] as

$$F = k_c z + \epsilon z^3 \quad (3.2)$$

The stiffness of the conical spring for the linear region is [33].

$$k_c = \frac{Gd^4}{2ND_{eq}^3} \quad (3.3)$$

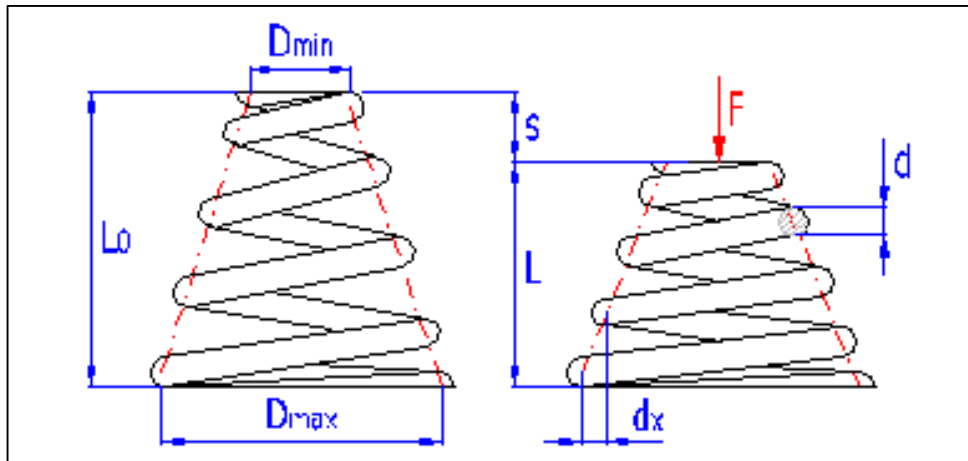


Figure 3.5. Geometric dimensions of a conical spring [33].

where D_{eq} is an equivalent mean coil diameter and is given by

$$D_{eq} = \sqrt[3]{(D_{max}^2 + D_{min}^2)(D_{max} + D_{min})} \quad (3.4)$$

The parameters for the above equations are given below.

G	Shear modulus of the spring material
d	Wire thickness of the spring
N	Number of active coils
D_{max}	Maximum mean coil diameter
D_{min}	Minimum mean coil diameter

3.2.2. Helical Springs

In helical springs the behavior is linear for most the region of operation and the force displacement relationship can be given using Hooke's law as

$$F = kz \quad (3.5)$$

where the spring constant k can be calculated using the formula given below.

$$k = \frac{Gd^4}{8D^3N} \quad (3.6)$$

where the parameters for the above equation are given below.

d	Wire thickness of the spring
G	Shear modulus of the spring material
D	Mean coil diameter
N	Number of active coils

3.2.3. Torsional Springs

Helical coil torsional springs force displacement relationship can be stated using Hooke's law

$$M = k_t \theta. \quad (3.7)$$

The angular stiffness can be calculated using the equation given below [34].

$$k_t = \frac{d^4 E}{64DN} \quad (3.8)$$

where the parameters for the above equation are given below.

d	Wire thickness of the spring
E	Young's modulus of the spring material
D	Mean coil diameter
N	Number of active coils

The number of active coils N_a is calculated using the formula shown below;

$$N = N_b + \frac{l_1 + l_2}{3\pi D} \quad (3.9)$$

N_b is the number of body turns and l_1 and l_2 are the moment arms lengths. N_b can be stated with the equation below.

$$N_b = N_c + \frac{\beta}{360} \quad (3.10)$$

where N_c is number of complete coils and β is the angle of rotation on incomplete coils.

3.3. RATCHETS AND SIMILAR ELEMENTS

Ratchets are used to transmit torque and rotation only in one direction. A ratchet cross section is given in Figure 3.6. in order to show the components of a ratchet.

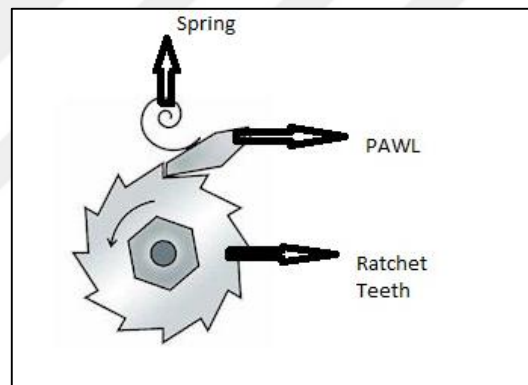


Figure 3.6. Sectional view of a ratchet and components [35]

The working principle of a ratchet is as follows. When the teeth turn in one direction the pawl permits motion and no torque is transmitted and a small resistive torque is developed. However, in the engagement direction the pawl locks together with the ratchet teeth and transmits the torque.

A drawback for ratchets is that in order to engage, the pawl must catch the teeth. In classical ratchet design, therefore, there is small amount of backlash in the engagement direction. Thus, such ratchets are not suitable for instantaneous engagement cases. Instead, one-way bearings or one-way clutches are preferred when the backlash is to be minimum. An example of a one-way bearing is shown in Figure 3.7.

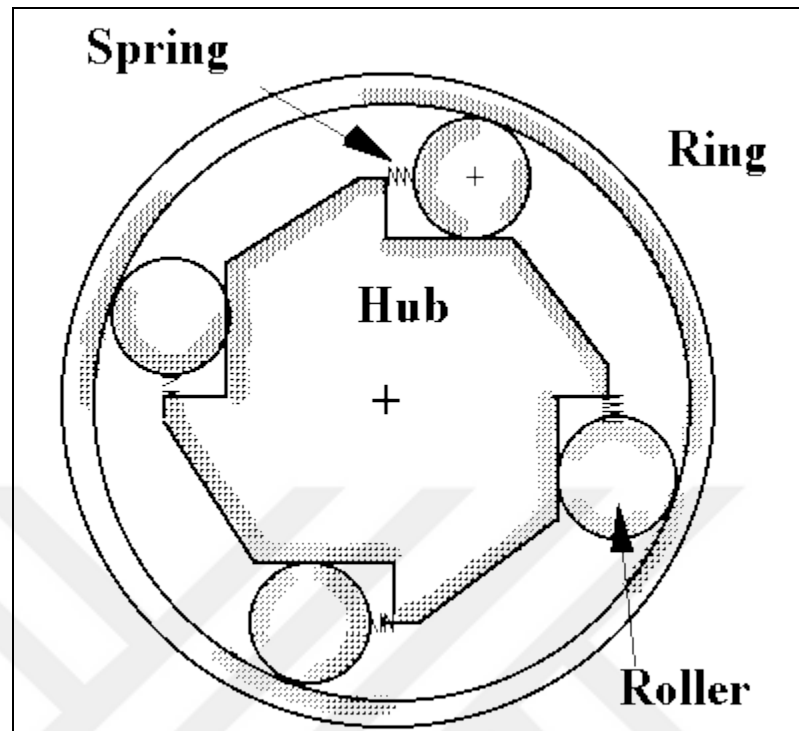


Figure 3.7. An example of a one-way bearing [36]

4. MODELING

In order to predict the motion of the system, accurate modeling is essential. In this study both static and dynamic model equations, including contact and impact dynamics, are developed. These models are then implemented in MATLAB in order to simulate the system behavior.

4.1. STATICS OF THE ENERGY HARVESTER

The static analysis of the design is done considering the assembly process. The rope is attached to the pulley at a reference position θ_{ref} which is taken as zero position for the pulley. This is shown in Figure 4.1.

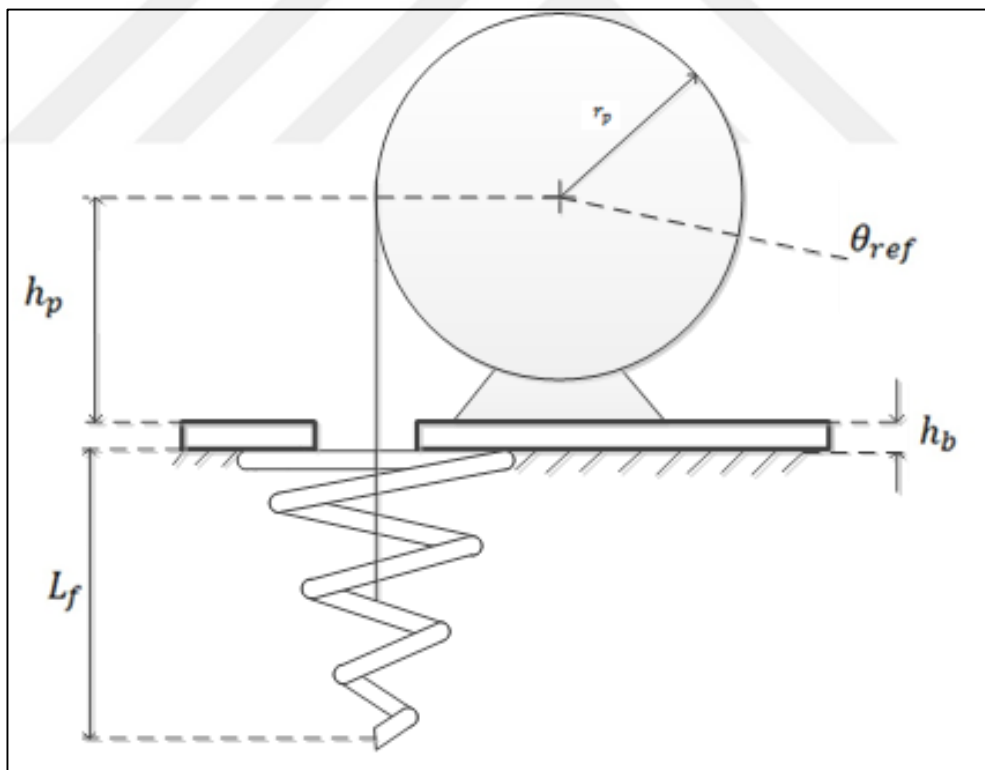


Figure 4.1. Assembly when the rope is connected to the pulley

The rope is rolled around the pulley and the angle the rope is rolled is represented as θ_{rope} .

There is a geometric condition for the rope to be tight when its end is connected to the conical spring which concerns the rope length L_r . This is given below.

$$L_r < H + \theta_{rope} r_p \quad (4.1)$$

In this equation H is the distance between the center of the pulley and the tip of the conical spring, which can be given as

$$H = h_p + h_b + L_f \quad (4.2)$$

When the connection of the rope to the tip of the conical spring is made the pulley rotates an angle θ_{ps} to its static equilibrium position and the spring compresses an amount of Δs to obtain its static equilibrium position. The position of the conical spring is measured from the free length of the conical spring. These are shown in Figure 4.2.

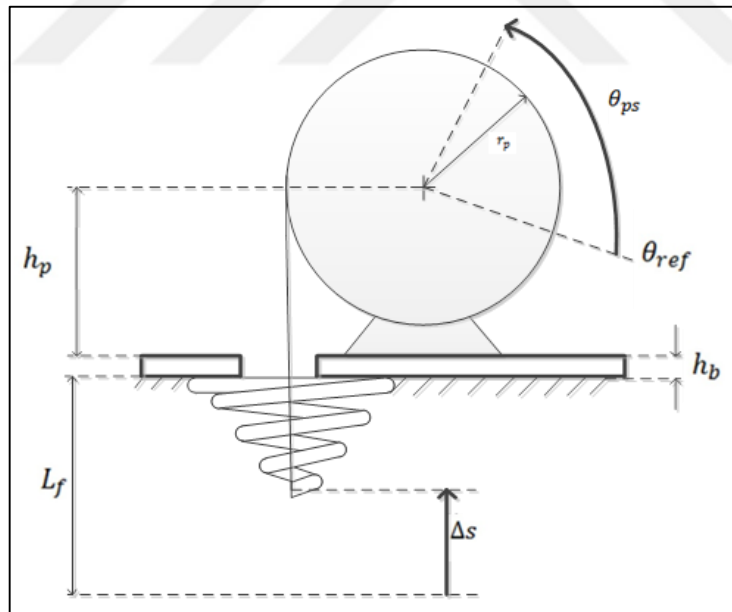


Figure 4.2. The pulley and conical spring static equilibrium positions after the rope is connected to the conical spring

To find the static equilibrium positions for the pulley and the tip of the conical spring, free body diagrams are drawn (Figure 4.3.).

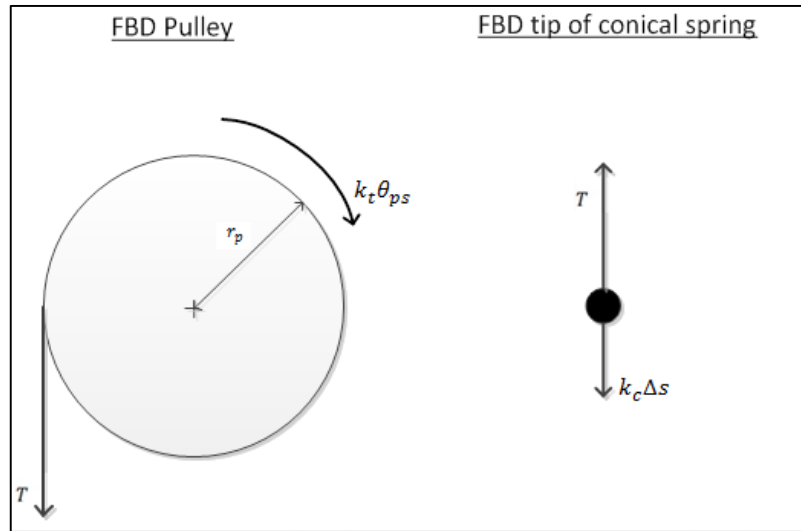


Figure 4.3. Free body diagrams of pulley and conical spring

Two static equilibrium equations are obtained from these diagrams as shown below.

$$k_t \theta_{ps} - T r_p = 0 \quad (4.3)$$

$$T - k_c \Delta s = 0 \quad (4.4)$$

There are three unknowns in the above equations, which are the static positions and the tensile force in the rope (θ_{ps} , Δs , T). Thus, to solve this problem another equation is required. This third equation comes from the geometry of the system due to the rope length being a constant and it is shown below where the total length of the rope is denoted as L_r .

$$L_f - \Delta s + H - L_f + r_p \theta_{rope} - r_p \theta_{ps} = L_r \quad (4.5)$$

Equation 4.5 reduces to the form shown below.

$$H + r_p \theta_{rope} - L_r = \Delta s + r_p \theta_{ps} \quad (4.6)$$

Solving equations 4.3, 4.4, 4.6 for Δs and θ_s and T , we obtain

$$\theta_{ps} = \frac{r_p}{k_t + r_p^2 k_c} (H + r_p \theta_{rope} - L_r) \quad (4.7)$$

$$\Delta s = \frac{k_t}{k_t + r_p^2 k_c} (H + r_p \theta_{rope} - L_r) \quad (4.8)$$

$$T = \frac{k_c k_t}{k_t + r_p^2 k_c} (H + r_p \theta_{rope} - L_r) \quad (4.9)$$

The next step in the assembly process is assembling the system into the tire with radius R . The geometry for this case is shown in Figure 4.4.

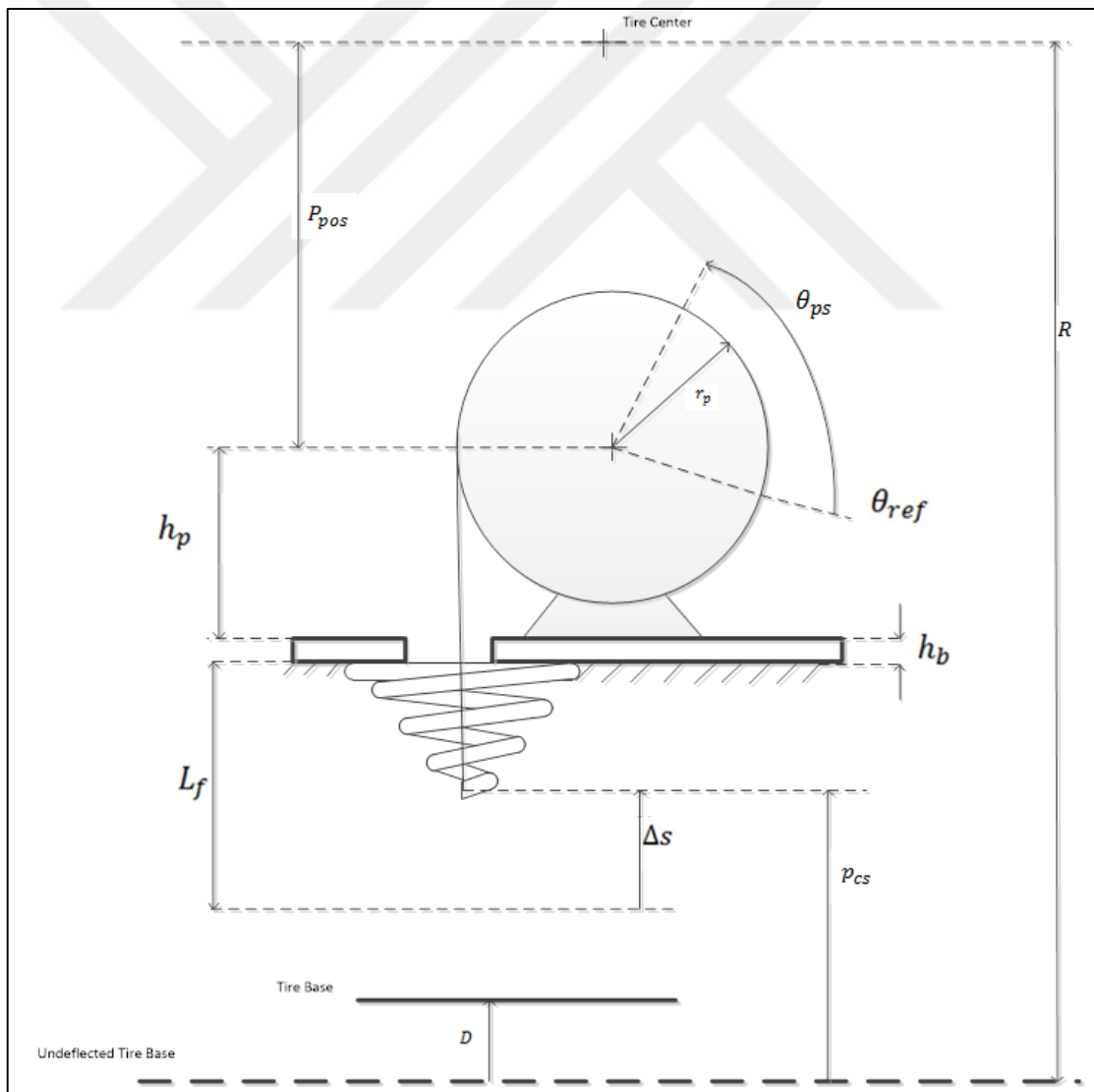


Figure 4.4. Assembly with tire base

The static position of the tip of the conical spring with respect to the undeflected tire base can be obtained as shown below.

$$p_{cs} = R - P_{pos} - H + \Delta s \quad (4.10)$$

A condition exists for the tip of the conical spring to have contact initially with the initial tire deflection position at D (see Section 4.2 for tire deflection model).

If $p_{cs} > D$, there is no contact between tire and tip of the conical spring thus the static positions of the system are found in Equations 4.7, 4.8, and 4.9.

$$p_{csf} = p_{cs} \quad (4.11)$$

$$\theta_{psf} = \theta_{ps} \quad (4.12)$$

If $p_{cs} < D$, then it is concluded that the tip of the conical spring will be in contact with the tire since it cannot penetrate the tire. Thus, the following calculations are made to find the new static equilibrium positions of the system.

$$p_{csf} = D \quad (4.13)$$

$$\theta_{psf} = \theta_{ps} - (D - p_{cs})r_p \quad (4.14)$$

Here another condition occurs for rope tightness. This is due to the change in the static position of the pulley as the conical spring is compressed to match the position of the tire. This condition for the rope to be tight is given as

$$\theta_{psf} > 0 \quad (4.15)$$

If this condition is not satisfied then $\theta_{psf} = 0$, since the rope cannot exert a negative moment on the pulley and thus cannot rotate it in the negative direction.

These values are referred to as static values with notation $p_{csf} = p_{cs}$ and $\theta_{psf} = \theta_{ps}$ in further sections of the thesis for convenience.

4.2. TIRE DEFLECTION MODELING

To simplify the tire deflection model an assumption is made that the only elastic deformation occurs in the contact patch and the rest of the tire is not affected from this deformation and stays the same. The geometry of contact patch with this assumption is shown in Figure 4.5.

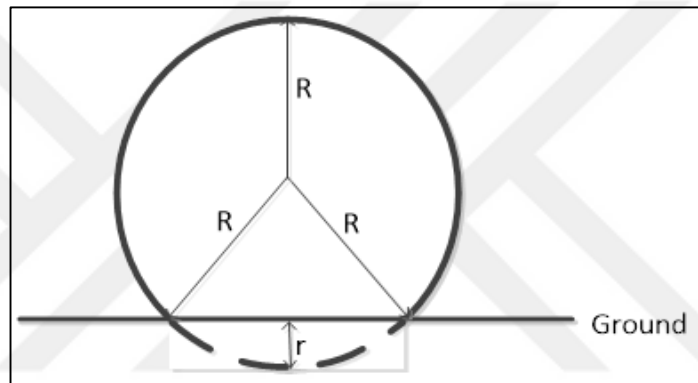


Figure 4.5. Simplified tire deflection model. The maximum deflection of the tire is r

The radial position of the tire surface can be written as a function of angular position θ . The total angle corresponding to the contact patch is denoted as β . These angles are shown in Figure 4.6.

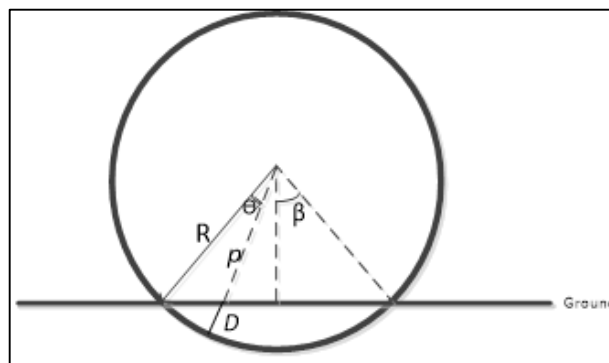


Figure 4.6. Contact patch angle and reference angle theta

The contact patch angle β in Figure 4.6. can be found as.

$$\beta = \cos^{-1}\left(\frac{R-r}{R}\right) \quad (4.16)$$

Therefore, from geometry, radial distance of a point on the tire to the tire center is

$$p = \begin{cases} \frac{R-r}{\cos(\beta-\theta)}, & 0 < \theta \leq \beta \\ R, & \beta < \theta \leq 2\pi \end{cases} \quad (4.17)$$

The radial deflection of the tire point shown in Figure 4.6. can be found by subtracting Equation 4.17 from the radius of the tire which yields the equation below

$$D = \begin{cases} R - \frac{R-r}{\cos(\beta-\theta)}, & 0 < \theta \leq \beta \\ 0, & \beta < \theta \leq 2\pi \end{cases} \quad (4.18)$$

The model given with Equation 4.18 is used to plot the radial deflection for a tire with radius of 22 cm and assumed maximum deflection of 2 cm. The angle β is calculated using Equation 4.16 as 0.451 radians. The graph of the radial deflection vs. the angular position is shown in the Figure 4.7.

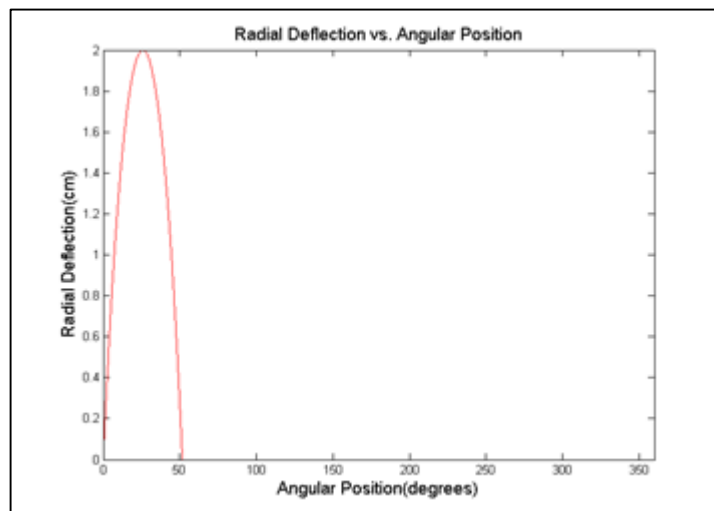


Figure 4.7. Radial deflection of tire vs. Angular position

The radial deflection model is dependent on the angular position but it is needed to be related to the vehicle velocity V . Therefore, a relationship between the vehicle velocity and angular position is needed. This is found by converting the vehicle velocity to angular velocity ω of the tire. The angular position is found by integrating ω . These relationships are given below.

$$\omega = \frac{V}{R} \quad (4.19)$$

$$\theta = \omega t \quad (4.20)$$

Thus, the radial deflection model which is a function of angular position becomes

$$D = \begin{cases} R - \frac{R-r}{\cos(\beta - \omega t)}, & 0 < t \leq \frac{\beta}{\omega} \\ 0, & \frac{\beta}{\omega} < t \leq \frac{2\pi}{\omega} \end{cases} \quad (4.21)$$

Using this equation the radial deflection velocity and acceleration can be calculated by taking derivatives with respect to time.

The radial deflection velocity of the tire is given below.

$$\frac{dD}{dt} = D_v = \begin{cases} \omega(R-r) \tan(\beta - \omega t) \sec(\beta - \omega t), & 0 \leq t \leq \frac{\beta}{\omega} \\ 0, & \frac{\beta}{\omega} < t \leq \frac{2\pi}{\omega} \end{cases} \quad (4.22)$$

The radial deflection acceleration of the tire is given below.

$$\frac{d^2D}{dt^2} = \frac{dD_v}{dt} = D_a \quad (4.23)$$

$$D_a = \begin{cases} -(R-r)\omega^2 \sec(\beta - \omega t)(1 + \tan^2(\beta - \omega t)), & 0 < t \leq \frac{\beta}{\omega} \\ 0, & \frac{\beta}{\omega} < t \leq \frac{2\pi}{\omega} \end{cases} \quad (4.24)$$

By using the same values as used previously for tire radius and maximum radial deflection, velocity and acceleration are found for given vehicle velocities. These are plotted in Figure 4.8. for 10 km/h vehicle speed. Other speed values yield similar plots.

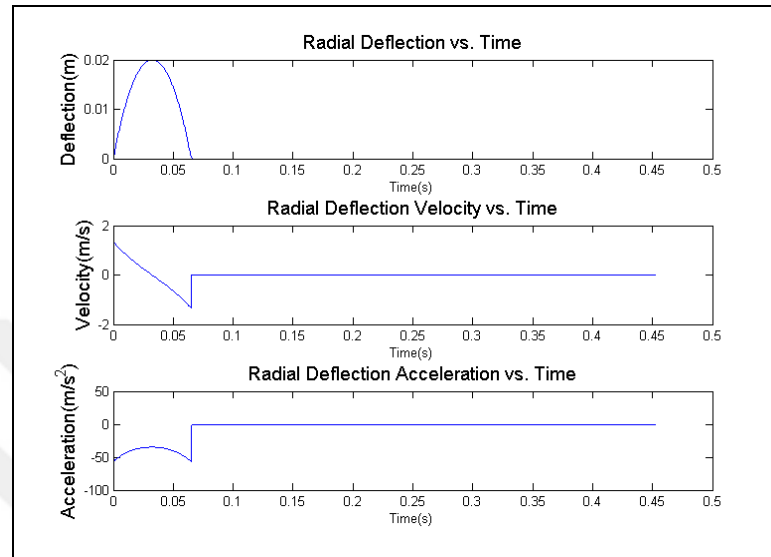


Figure 4.8. The radial deflection, velocity and acceleration at 10 km/h.

The radial deflection velocity and acceleration changes as a function of vehicle velocity. This behavior is shown in Figure 4.9.

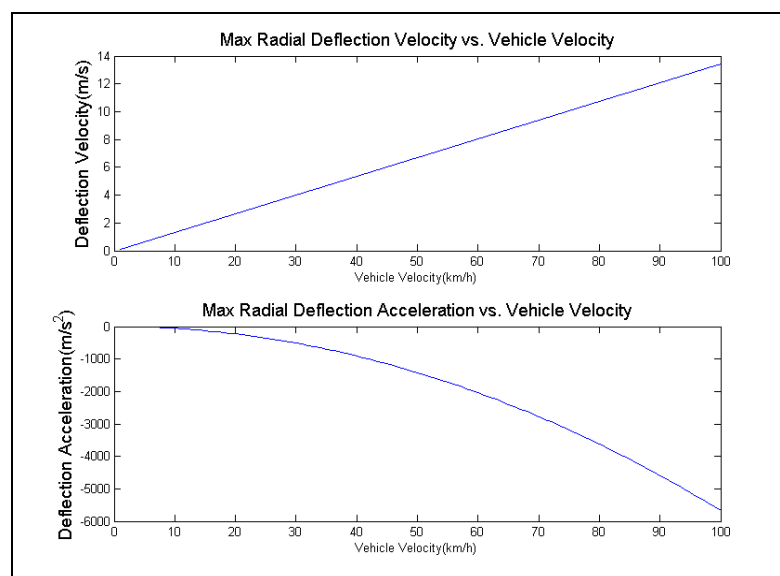


Figure 4.9. Maximum radial deflection velocity and acceleration vs. vehicle velocity

From Equation 4.22, the maximum radial deflection velocity is linearly related to the vehicle velocity. Figure 4.8. shows that this equation is maximum when $t = 0$ with a value of

$$D_{v,max} = \omega(R - r) \tan(\beta) \sec(\beta) \quad (4.25)$$

where $\tan(\beta)$ and $\sec(\beta)$ can be found using the geometry shown in Figure 4.6.

$$\tan(\beta) = \frac{\sqrt{R^2 - (R - r)^2}}{R - r} \quad (4.26)$$

$$\sec(\beta) = \frac{R}{R - r} \quad (4.27)$$

Plugging $\omega = \frac{V}{R}$, and, Equations 4.26 and 4.27 into Equation 4.25, one gets

$$D_{v,max} = \frac{V}{R} (R - r) \frac{\sqrt{R^2 - (R - r)^2}}{R - r} \frac{R}{R - r} \quad (4.28)$$

After the equation is simplified the relationship between the maximum radial deflection velocity and vehicle velocity is obtained

$$D_{v,max} = \frac{\sqrt{R^2 - (R - r)^2}}{R - r} V = \left(\sqrt{\left(\frac{R}{R - r} \right)^2 - 1} \right) V = \tan(\beta) V \quad (4.29)$$

Since all the parameters are constant it is proven that the relationship between the vehicle velocity and maximum radial deflection velocity is linear. For example, for a vehicle speed of 50 km/h, the max radial deflection velocity is 6.36 m/s .

In the next section the conical spring is modeled as a spring with an equivalent tip mass and the governing equation of the conical spring is determined.

4.3. CONICAL SPRING WITH EQUIVALENT MASS MODELING

In order to simplify the equation of motion for the deflection of the tip of a conical spring, the spring is modeled as a massless conical spring with an equivalent point mass at the tip. This is shown in the Figure 4.10.

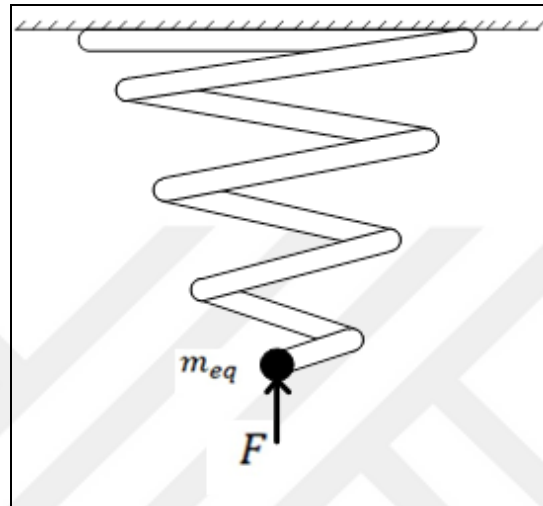


Figure 4.10. Conical spring with equivalent tip mass

The equation of motion of the tip can be written simply as shown below for positive z axis of motion pointing upwards;

$$m_{eq}\ddot{z} + b\dot{z} + kz = F \quad (4.30)$$

The parameters in the above equation are given as;

m_{eq}	Equivalent mass of the conical spring
b	Equivalent viscous damping coefficient
k	Stiffness of the conical spring
F	Force applied to the tip

The total mass of the conical spring can be found by integrating the infinitesimal mass over the whole spring;

$$m = \int dm = \rho A \int ds \quad (4.31)$$

where

ρ	Density of the material of the conical spring
A	The cross sectional area of the spring
ds	Infinitesimal length of the spring

In order to find the equivalent mass of the conical spring kinetic energy equivalence method is used. This is done considering the experimental setup in which the system does not rotate (Section 6). Therefore, the calculation can be based on an inertial coordinate system in which the spring moves. For kinetic energy equivalence, first the kinetic energy of the spring is calculated. Then the kinetic energy of an equivalent mass at tip, moving at tip velocity is calculated. By equating these two the equivalent mass is solved.

$$T_{meq} = T_{tot} \quad (4.32)$$

where the total kinetic energy is given as

$$T_{tot} = \int \frac{1}{2} (V(s))^2 dm = \frac{1}{2} \rho A \int (V(s))^2 ds \quad (4.33)$$

In this case the position of the equivalent point mass is chosen as the tip of the conical spring and it is known that the velocity is maximum at this point. Thus the Equation 4.32 becomes

$$\frac{1}{2} m_{eq} V_{max}^2 = \frac{1}{2} \rho A \int (V(s))^2 ds \quad (4.34)$$

Now

$$ds = \sqrt{dx^2 + dy^2 + dz^2} \quad (4.35)$$

The values for dx , dy and dz are obtained using the geometry of the conical spring which is shown in Figure 4.11.

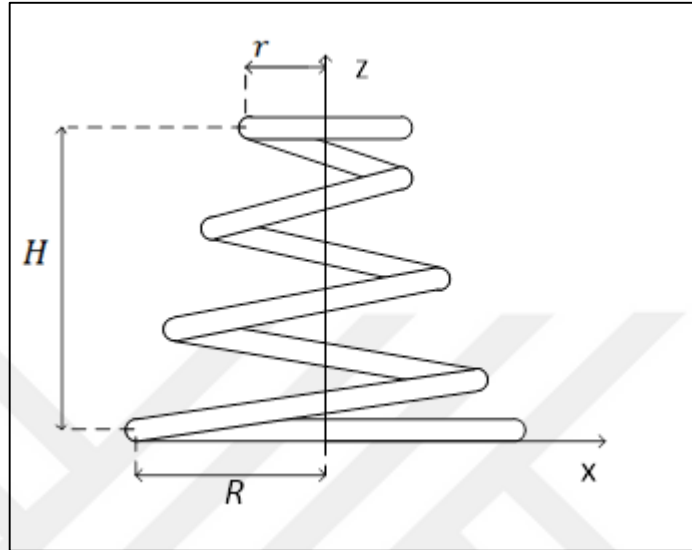


Figure 4.11. Dimensions of a conical spring

x , y and z coordinates for determining the infinitesimal elements in the conical spring are found as shown below;

$$x = (R - \alpha z)\cos(\theta) \quad (4.36)$$

$$y = (R - \alpha z)\sin(\theta) \quad (4.37)$$

$$z = \mu\theta \quad (4.38)$$

The mathematical representations for α and μ are

$$\alpha = \tan(\gamma) = \frac{R - r}{H} \quad (4.39)$$

$$\mu = R\tan(\psi) \quad (4.40)$$

Figure 4.12. shows the helix angle, the cone angle, and the pitch.

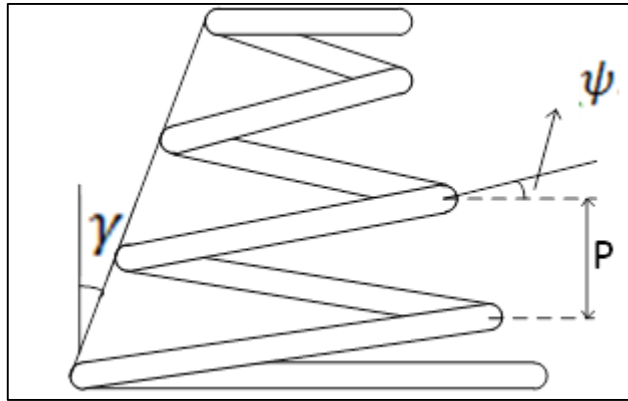


Figure 4.12. Cone angle, pitch and inclination angle

The helix angle ψ can be calculated using the pitch P of the conical spring as shown below

$$\psi = \tan^{-1} \frac{P}{2\pi R} \quad (4.41)$$

Equation 4.38 is plugged into the equations 4.36 and 4.37, and the derivatives with respect to θ are used to obtain the resulting equations for dx , dy and dz .

$$dx = [-\alpha\mu\cos(\theta) + (R - \alpha\mu\theta)\sin(\theta)]d\theta \quad (4.42)$$

$$dy = [-\alpha\mu\sin(\theta) - (R - \alpha\mu\theta)\cos(\theta)]d\theta \quad (4.43)$$

$$dz = kd\theta \quad (4.44)$$

Plugging in dx , dy and dz in to Equation 4.35 ds is found.

$$ds = \sqrt{(R - \mu\theta\alpha)^2 + \mu^2(\alpha^2 + 1)}d\theta \quad (4.45)$$

The total length of the spring is found by integrating ds over the whole spring.

$$s = \int_0^{\theta_{max}} ds \quad (4.46)$$

$$s = \frac{1}{2} \frac{R}{\alpha \tan \psi} \left(K^2 \ln \left(\frac{\sqrt{K^2 + u^2} + u}{\sqrt{K^2 + R^2} - R} \right) + u \sqrt{K^2 + u^2} + \sqrt{K^2 + 1} \right) \quad (4.47)$$

The terms K and u are constants used to simplify the expression. These constants are given below.

$$K = \tan \psi \sqrt{\alpha^2 + 1} \quad (4.48)$$

$$u = \alpha \theta_{max} \tan \psi - 1 \quad (4.49)$$

Using Equation 4.31 and Equation 4.47 total mass of the conical spring is found as

$$m = \frac{1}{2} \frac{\rho A R}{\alpha \tan \psi} \left(K^2 \ln \left(\frac{\sqrt{K^2 + u^2} + u}{\sqrt{K^2 + 1} - 1} \right) + u \sqrt{K^2 + u^2} + \sqrt{K^2 + 1} \right) \quad (4.50)$$

In order to calculate the solution to the integral for T_{tot} in Equation 4.33 the velocity profile must be included to the calculations. The velocity profile assumed is linear and it is shown in Figure 4.13.

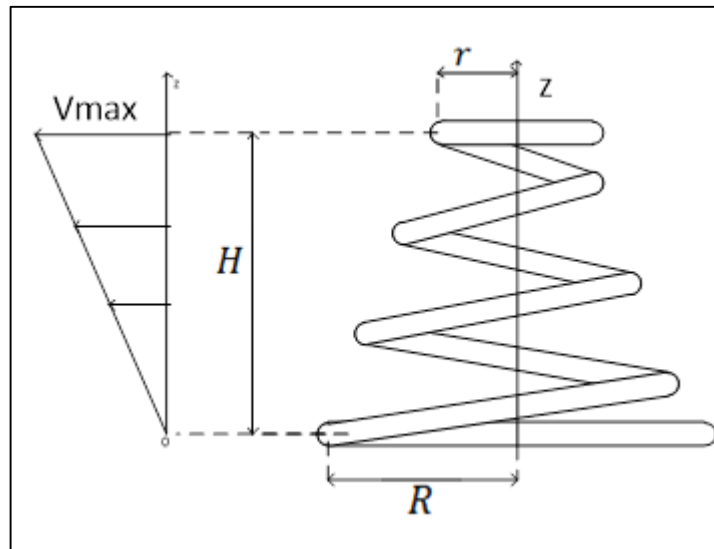


Figure 4.13. Velocity profile of the conical spring

The equation for the velocity profile is given as below;

$$V = \frac{z}{H} V_{max} = \frac{\mu\theta}{H} V_{max} \quad (4.51)$$

Plugging in this velocity profile and ds in to Equation 4.33. T_{tot} is obtained by carrying out the integration

$$T_{tot} = \frac{1}{2} \rho A \left(\frac{\mu V_{max}}{H} \right)^2 \int_0^{\theta_{max}} \theta^2 \sqrt{(R - \mu\theta\alpha)^2 + \mu^2(\alpha^2 + 1)} d\theta \quad (4.52)$$

Which yields the total kinetic energy as

$$\begin{aligned} T_{tot} = \frac{1}{2} \rho A \left(\frac{V_{max}}{H} \right)^2 \frac{R^3}{\tan\psi\alpha^3} & \left[\frac{1}{8} (K^2 \right. \\ & - 4) \left(K^2 \ln \left(\frac{\sqrt{K^2 + 1} - 1}{\sqrt{K^2 + u^2} + u} \right) - u\sqrt{K^2 + u^2} - \sqrt{K^2 + 1} \right) \\ & \left. + \frac{1}{12} (8 + 3u)(K^2 + u^2)^{\frac{3}{2}} - \frac{5}{12} (K^2 + 1)^{\frac{3}{2}} \right] \quad (4.53) \end{aligned}$$

Using T_{tot} in Equation 4.34, m_{eq} is found as

$$\begin{aligned} m_{eq} = \frac{\rho AR^3}{H^2 \alpha^3 \tan\psi} & \left[\frac{1}{8} (K^2 \right. \\ & - 4) \left(K^2 \ln \left(\frac{\sqrt{K^2 + 1} - 1}{\sqrt{K^2 + u^2} + u} \right) - u\sqrt{K^2 + u^2} - \sqrt{K^2 + 1} \right) \\ & \left. + \frac{1}{12} (8 + 3u)(K^2 + u^2)^{\frac{3}{2}} - \frac{5}{12} (K^2 + 1)^{\frac{3}{2}} \right] \quad (4.54) \end{aligned}$$

The ratio between the equivalent mass and the total mass which is of significance can be found by dividing Equation 4.54 by Equation 4.50. The resulting formula for this ratio is

$$\begin{aligned}
m_{ratio} &= \frac{m_{eq}}{m} \\
&= \left(\frac{R}{R-r}\right)^2 \frac{f}{K^2 \ln\left(\frac{\sqrt{K^2+u^2}+u}{\sqrt{K^2+1}-1}\right) + u\sqrt{K^2+u^2} + \sqrt{K^2+1}}
\end{aligned} \tag{4.55}$$

where f is

$$\begin{aligned}
f &= \frac{1}{8}(K^2 - 4) \left(K^2 \ln\left(\frac{\sqrt{K^2+1}-1}{\sqrt{K^2+u^2}+u}\right) - u\sqrt{K^2+u^2} - \sqrt{K^2+1} \right) \\
&\quad + \frac{1}{12}(8+3u)(K^2+u^2)^{\frac{3}{2}} - \frac{5}{12}(K^2+1)^{\frac{3}{2}}
\end{aligned} \tag{4.56}$$

To observe the effect of cone angle, m_{ratio} is solved for a range from zero degrees to ninety degrees of cone angle. This was obtained by changing the small radius r in the range of zero to the large radius R . The numerical values for the parameters used for the solution are given as large radius $R = 0.1 \text{ m}$, pitch of the spring $P = 0.01 \text{ m}$ and height of the spring as $H = 0.1 \text{ m}$. Note that the mass ratio is independent of wire size and density. The resulting graph is shown in Figure 4.14.

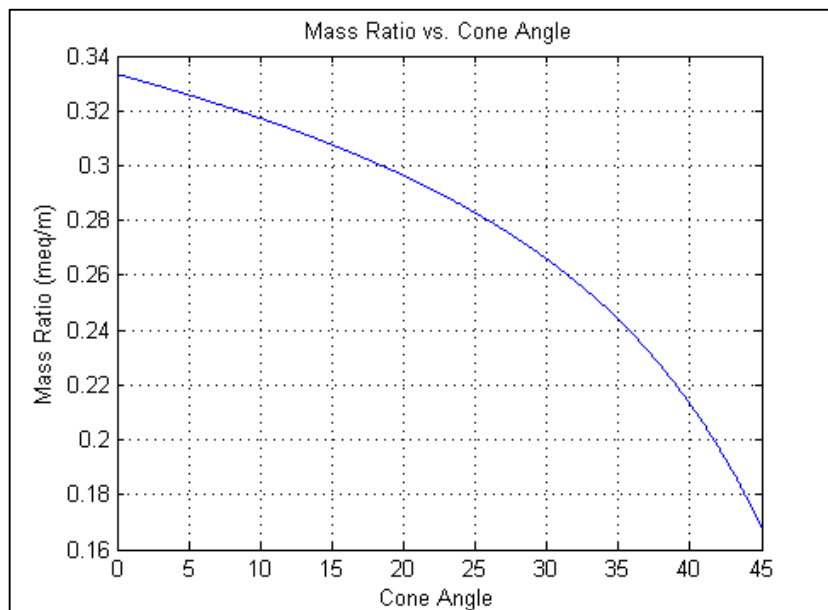


Figure 4.14. Mass Ratio vs. Cone Angle graph by variation in small radius

It is known that in helical springs the mass ratio is equal to $1/3$ [37]. This can be seen by looking at the case where the cone angle is zero where the mass ratio is observed to be 0.333. It is also seen that the mass ratio decreases as the cone angle increase.

In order to observe the deflection behavior of a conical spring under static loading conditions and in order to find the relation between the applied force and the deflection of the conical spring a solid model is created using SolidWorks software. The model of the conical spring is shown in Figure 4.15.

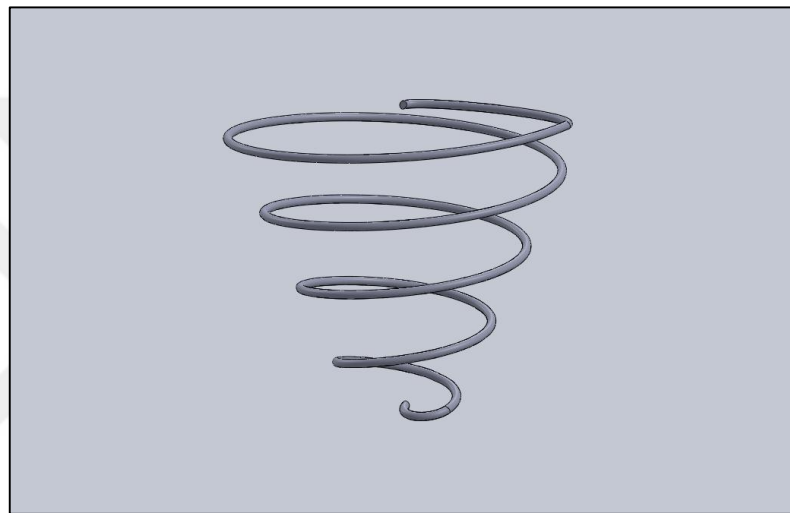


Figure 4.15. Solid Model of conical spring

The dimensions of the solid model are as shown in Table 4.1.

Table 4.1. Dimensions of the solid model conical spring

Cone Angle (degrees)	Height (mm)	Small Radius (mm)	Large Radius (mm)	wire Thickness (mm)
25	180	30	113.94	5

This model is used to numerically solve the deflection of the conical spring under an applied load. This was done using SolidWorks software.

AISI 1020 cold rolled steel was used as the material of the solid model. The properties of this material are given in Table 4.2.

Table 4.2. Material properties of AISI 1020 cold rolled steel

AISI 1020 cold rolled steel	
Modulus of Elasticity (GPa)	205
Poissons Ratio	0.29
Shear Modulus (Gpa)	80
Density (kg/m ³)	7870

A fixed boundary condition was applied to the top part of the conical spring to prevent motion in any direction. This is shown in Figure 4.16.

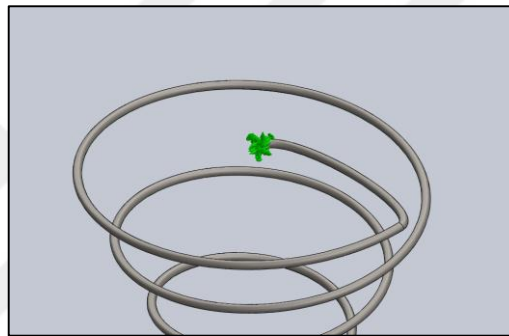


Figure 4.16. Boundary conditon on the conical spring

A vertical compressive load was applied to the tip of the conical spring which is shown in Figure 4.17.

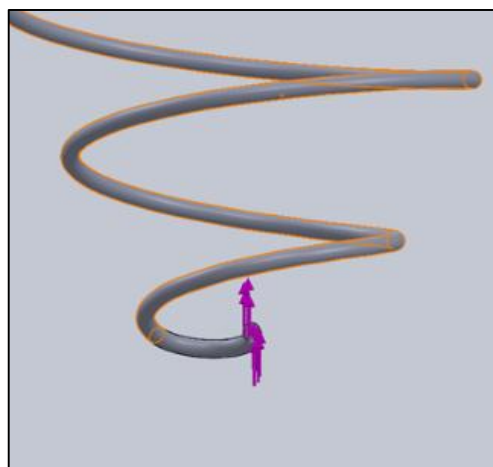


Figure 4.17. Force applied to the tip of the conical spring

The solution is done for a range of forces applied to the tip of the spring using large displacement analysis in SolidWorks. The forces applied are given in Table 4.3.

Table 4.3. The values of applied forces

Applied Force(N)
0.1
1
3
5
10
15
20
25
30

The results obtained for the displacement of the tip of the spring are given in Table 4.4.

Table 4.4. Applied forces and obtained tip displacements

Applied force(N)	SolidWorks (Large Displacement)
0.1	0.4014
1	3.832
3	12.09
5	20.2
10	40.88
15	62.97
20	-
25	-
30	-

It was seen that SolidWorks was not able to solve the problem after fifteen newtons of applied force. Thus ANSYS software was used to obtain another set of solutions for the same applied loads. The same steps which are done to compute the solution using SolidWorks are done and the results obtained are given in Table 4.5.

Table 4.5. Results for displacement obtained by using ANSYS

Applied Force(N)	Displacement(mm)
0.1	0.40909
1	4.0909
3	12.273
5	20.454
10	40.909
15	61.363
20	81.818
25	102.27
30	122.73

It is seen that ANSYS was able to calculate for all the loading cases.

In Figure 4.18. both ANSYS and SolidWorks are plotted in the same graph. From this graph it is seen that the results obtained from both software are nearly the same. Therefore the computational errors are assumed to be negligible.

It can be seen that the graph is linear. Thus it can be said that the spring behaves linearly in this region. Since no data has been obtained beyond this, the end of the linear region is not determined. However, from the data the linear range can be said to be above 68.2% of the height of the spring.

A curve fitting is applied to the results obtained by ANSYS since it has a larger data set. The result for this linear curve fit is shown below;

$$F = 0.244z$$

The R-squared value for this fit is 1. This means almost a perfect fit. By using this equation it can be said that the spring constant is 0.244 N/mm for this particular conical spring.

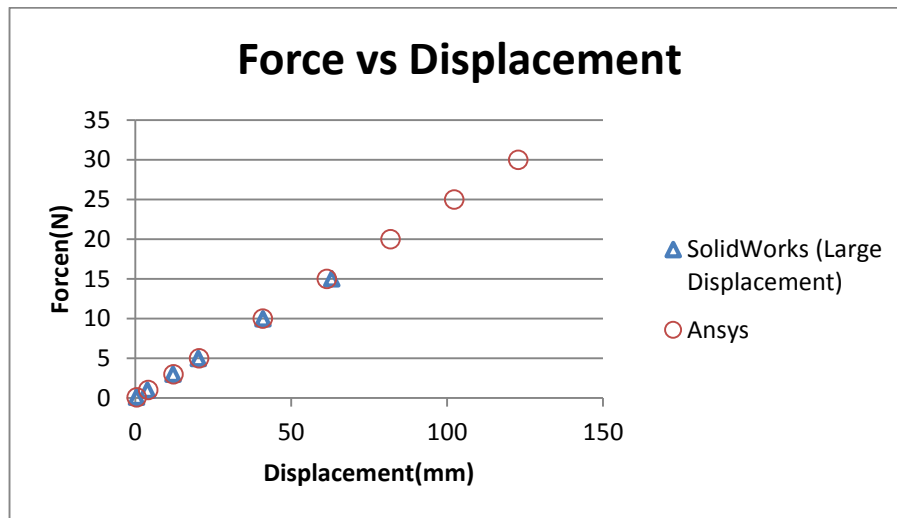


Figure 4.18. Results obtained by SolidWorks and ANSYS software

4.3.1. Dynamics of the Conical Spring

As stated in finding the equivalent mass, the equation of motion of the tip of the conical spring is simplified to the form given in Equation 4.30. It is seen that this is a basic spring mass damper system with a forced excitation.

The natural frequency, the damped natural frequency and the damping ratio of this system are given as below;

$$\omega_n = \sqrt{\frac{k}{m_{eq}}} \quad (4.57)$$

$$\zeta = \frac{b}{2m_{eq}\omega_n} \quad (4.58)$$

$$\omega_d = \sqrt{\frac{k}{m_{eq}}} \sqrt{1 - \left(\frac{b}{2m_{eq}\omega_n}\right)^2} \quad (4.59)$$

The natural frequency of the spring analyzed in ANSYS and SolidWorks in the previous section is calculated as 46.9 Hz.

4.4. PULLEY MODEL

The pulley assembly consists of two parts. The first part is the pulley itself and the second part is the shaft which is the pulley attached on. These two parts are shown in Figure 4.19.

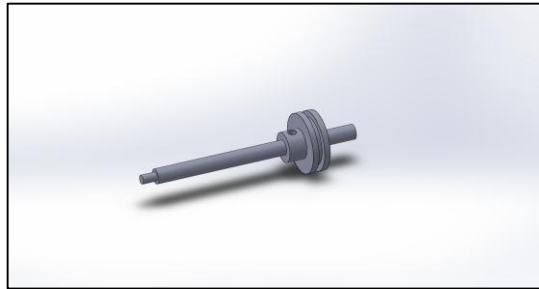


Figure 4.19. The pulley attached to the shaft

The pulley has a radius r_p and a torsional spring is attached to the pulley with spring coefficient of k_t . This generates a torque proportional to the angular position of the pulley considering the initial position where the spring is unstretched as zero. The torque is obtained from Hooke's law shown below, where the position of the pulley is given as θ_p ;

$$\tau_{spr} = \theta_p k_t \quad (4.60)$$

The pulley is driven by the tension T , which is created by the rope attached to it and the shaft is subjected to a torque M , which is the load moment responsible for coupling with the other parts the shaft is attached to. This is shown in Figure 4.20.

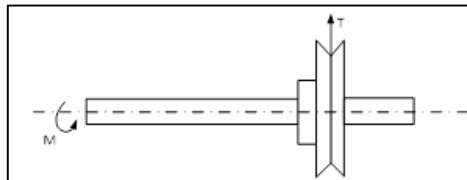


Figure 4.20. Pulley diagram with forces and moments

The pulley has a mass moment of inertia as I_p and the shaft has a mass moment of inertia I_s .

Thus the free body diagram of the pulley is found as shown in Figure 4.21.

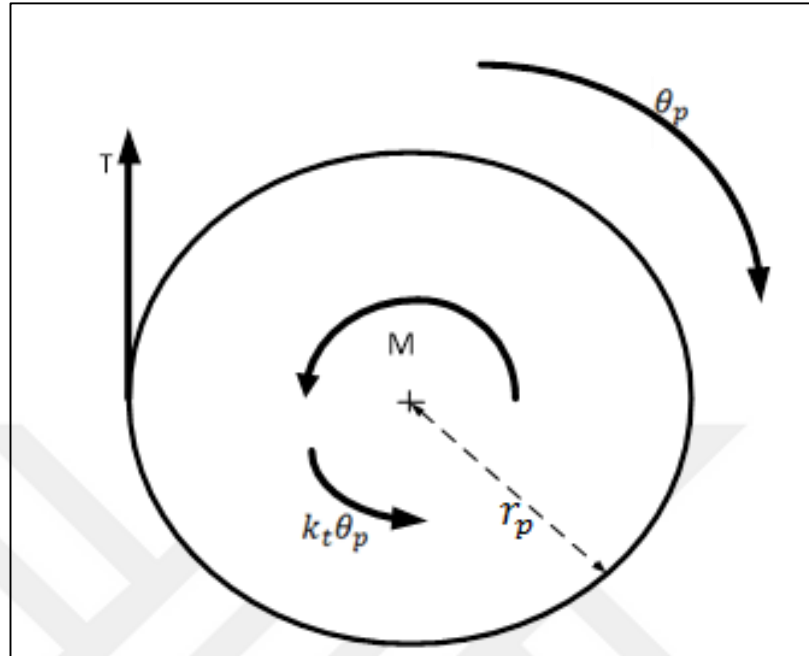


Figure 4.21. Free body diagram of pulley

The governing dynamical equation is found as shown below;

$$(I_p + I_s)\ddot{\theta}_p + b\dot{\theta}_p + k_t\theta_p = Tr_p - M \quad (4.61)$$

where b is the total viscous damping of the pulley and the shaft. This term can be neglected if necessary since viscous damping can be assumed to be very low.

It can be seen here that the system is a second order spring mass damper system. The natural frequency, damped natural frequency and the damping ratio are given below;

$$\omega_n = \sqrt{\frac{k_t}{(I_p + I_s)}} \quad (4.62)$$

$$\zeta = \frac{b}{2(I_p + I_s)\omega_n} \quad (4.63)$$

$$\omega_d = \sqrt{\frac{k_t}{(I_p + I_s)}} \sqrt{1 - \left(\frac{b}{2(I_p + I_s)\omega_n}\right)^2} \quad (4.64)$$

4.5. GENERATOR MODELING AND CHARACTERIZATION

In this project, a DC motor is used a generator. DC motors are driven by an external voltage source. They are governed by two coupled differential equations, one of which is for the mechanical part and the other is for the electrical part. These equations are given below.

$$J\dot{\omega} + b\omega = k_t i - M \quad (4.65)$$

$$L \frac{di}{dt} + Ri = V - k_b \omega \quad (4.66)$$

The parameters for the above equations are

J	Inertia of the DC motor
b	Viscous damping
k_t	Torque constant
L	Inductance
$R = R_m + R_{load}$	Total resistance which equals the summation of coil resistance and load resistance (if any)
k_b	Back EMF constant
M	Driving torque
V	Voltage between motor terminals

When the DC motors are used as generators the driving terms change. Generators are governed by the same differential equations with modified signs for the driving and the load terms.

$$J\dot{\omega} + b\omega = -k_t i + M \quad (4.67)$$

$$L \frac{di}{dt} + Ri = -V + k_b \omega \quad (4.68)$$

The generator modeling is done using the generator equations for a closed circuit where no external voltage source is used. This crosses out the V term in the above equations. The electrical constant is equal to the torque constant which is also called motor constant ($k_t = k_b = k$). Hence, the Equations 4.67 and 4.68 reduce to the form shown below.

$$J\dot{\omega} + b\omega = -ki + M \quad (4.69)$$

$$L \frac{di}{dt} + Ri = k\omega \quad (4.70)$$

In order to decouple this differential equation system, ω terms can be written in terms of i using Equation 4.70, which yields

$$\omega = \frac{L \frac{di}{dt} + Ri}{k} \quad (4.71)$$

$$\dot{\omega} = \frac{L \frac{d^2i}{dt^2} + R \frac{di}{dt}}{k} \quad (4.72)$$

When above equations are used in Equation 4.69 a second order differential equation is obtained for i .

$$LJ \frac{d^2i}{dt^2} + (Lb + RJ) \frac{di}{dt} + (k^2 + Rb)i = kM \quad (4.73)$$

The same method can be applied to find the decoupled differential equation of ω . The i terms can be written in terms of ω using Equation 4.69 which are given below;

$$i = \frac{M - J\dot{\omega} - b\omega}{k} \quad (4.74)$$

$$\frac{di}{dt} = \frac{-J\ddot{\omega} - b\dot{\omega}}{k} \quad (4.75)$$

Using above equations in Equation 4.70 gives the second order differential equation for ω as follows.

$$LJ\ddot{\omega} + (Lb + RJ)\dot{\omega} + (k^2 + Rb)\omega = RM \quad (4.76)$$

Both Equation 4.73 and 4.76 are second order differential equations and have the same coefficients which are the equivalent mass LJ , the equivalent damping $(Lb + RJ)$ and the equivalent spring constant $(k^2 + Rb)$. It is seen that the equations being of second order is caused by including the inductance of the DC motor since the inertia cannot be neglected. Thus it can be said that the inductance of the DC motor induces a second pole on the system which may cause oscillation if the system is critically or under damped.

Equations 4.69 and 4.70 can be solved using state space method. This is done for when the motor is not driven by any external torque ($M = 0$).

State vector is given as

$$S = \begin{bmatrix} \omega \\ i \end{bmatrix} \quad (4.77)$$

The system reduces to the form given below.

$$\dot{S} = A S \quad (4.78)$$

where the matrix A is

$$A = \begin{bmatrix} -\frac{b}{j} & -\frac{k}{j} \\ \frac{k}{L} & -\frac{R}{L} \end{bmatrix} \quad (4.79)$$

The solution to Equation 4.78 is well-known:

$$S = e^{At} S_0 \quad (4.80)$$

where S_0 is the state vector at $t = 0$.

As it is seen, there are five different parameters governing the generator equations: J , b , k , L and R_m . These parameters have to be determined in order to fully characterize the DC motor.

The DC motor to be characterized and used in the experiments is chosen as Mabuchi RS-360SH (Figure 4.22.). During the characterization process the motor is driven mostly by an external voltage source. Thus the DC motor equations are applicable.



Figure 4.22. Mabuchi RS-360SH DC motor

4.5.1. Internal Resistance

The internal resistance R_m of the DC motor is measured by using a multi-meter in ohmmeter mode. The measurement was repeated a few times. The average result is

$$R_m = 22.9 \Omega$$

with negligible variance.

4.5.2. Motor Constant

In order to measure the motor constant k , the relationship between the back EMF (voltage induced due to the rotation without external voltage) and angular speed is used. This relation is

$$k\omega = V_{emf} \tag{4.81}$$

However, measuring V_{emf} is difficult because without an external voltage the motor will continuously slow down due to damping. Nevertheless, when the motor is supplied a constant voltage after a period of time the back EMF will cancel the supplied voltage ($V = V_{emf}$) and the motor will reach a steady state. Therefore, for a motor running at constant speed under an external voltage V , $k\omega = V$.

An experiment is conducted to obtain the data required. A power supply is used for a constant voltage input to the motor. After the steady state is reached the rotor angular speed and the current is measured. For angular speed a tachometer is used. Current is read directly from the power supply.

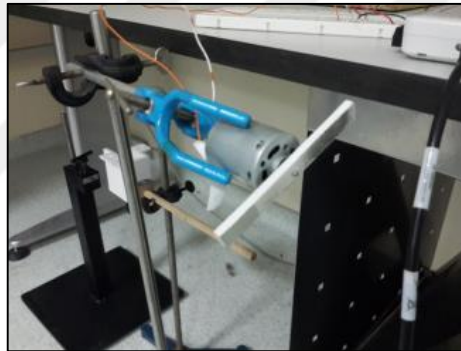


Figure 4.23. Rectangular part attached to shaft of motor

A rectangular part is mounted to the shaft of the motor, Figure 4.23, on which a reflective patch is placed. The optical tachometer measures the frequency of the shaft rotation based on the light pulses reflected from the patch. For reliability, the current is also measured by using a multimeter.

This experiment is conducted for supply voltages ranging from 2 V (for the motor to work properly) to 12 V. The collected experimental data is shown in Table 4.6 where the frequency of rotation is converted from RPM to rad/s. The data obtained is then plotted in Figure 4.24.

Table 4.6. Voltage and angular velocity data

Voltage (V)	Average Current (mA)	Angular Velocity (rad/s)
2	48.00	79.59
3	49.33	168.70
4	50.67	251.01
5	52.67	335.10
6	55.67	407.78
7	59.33	490.09
8	63.33	564.23
9	68.33	647.27
10	73.33	726.13
11	79.67	795.87
12	85.67	869.17

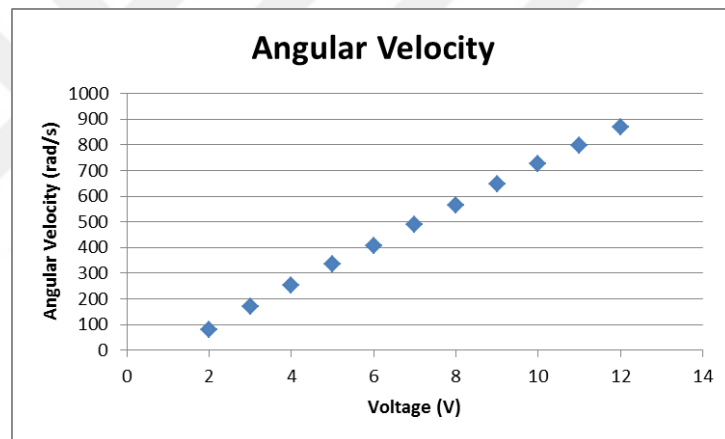


Figure 4.24. Voltage vs. angular velocity graph

It can be seen that the relationship is linear as expected. However, in order to get rid of any unwanted nonlinearity effects at low velocities, a linear regression is applied to the data for 5-12 V, with intercept at origin. The result is the following.

$$\omega = 71.702V \quad (4.82)$$

The correlation coefficient of the fit is found as 0.9943. Thus motor constant k is found as

$$k = \frac{1}{71.702} = 0.0139 \frac{\text{Vs}}{\text{rad}}$$

4.5.3. Damping Coefficient

At steady state the mechanical equation for the DC motor reduces to the following.

$$b\omega = ki \quad (4.83)$$

The damping is then obtained as shown below.

$$b = \frac{ki}{\omega} = \frac{k^2i}{V} = 1.9321 \times 10^{-4} \frac{i}{V} \quad (4.84)$$

Therefore, in order to calculate the damping coefficient b , the current and voltage data in Table 4.6 can be used in Equation 4.84. The calculated damping data is presented in Table 4.7 and then plotted versus angular speed (Figure 4.25.).

Table 4.7. Calculated angular velocity and damping data

Angular Velocity (rad/s)	Damping (N m s/rad)
143.40	4.67E-06
215.11	3.20E-06
286.81	2.46E-06
358.51	2.05E-06
430.21	1.80E-06
501.91	1.65E-06
573.62	1.54E-06
645.32	1.48E-06
717.02	1.43E-06
788.72	1.41E-06
860.42	1.39E-06
932.126	1.35E-06
1003.828	1.37E-06
1075.53	1.37E-06
1147.232	1.39E-06

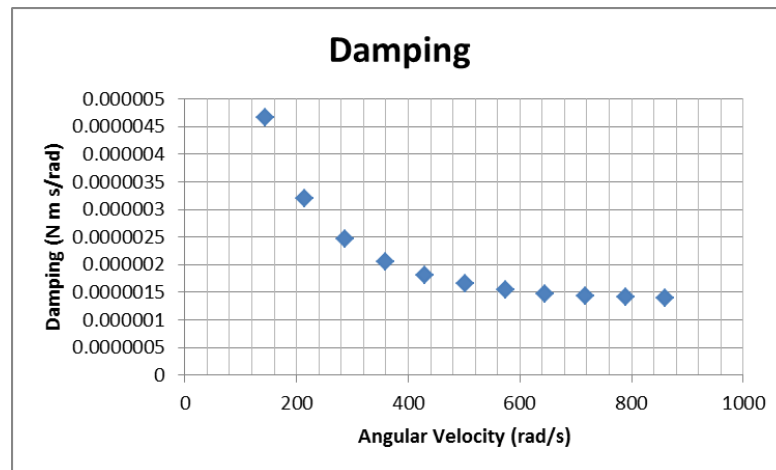


Figure 4.25. Damping vs. angular velocity

Although the graph shows the behavior of the damping more data is needed to be sure that the behavior does not change in higher angular velocities and if no change occurs to see the steady state value clearly. In order to do this more data is collected for current from 12 V up to 16 V in one volt increments.

After the same calculations for angular velocity and damping are made, the extended data are plotted again and the graph is given in Figure 4.26.

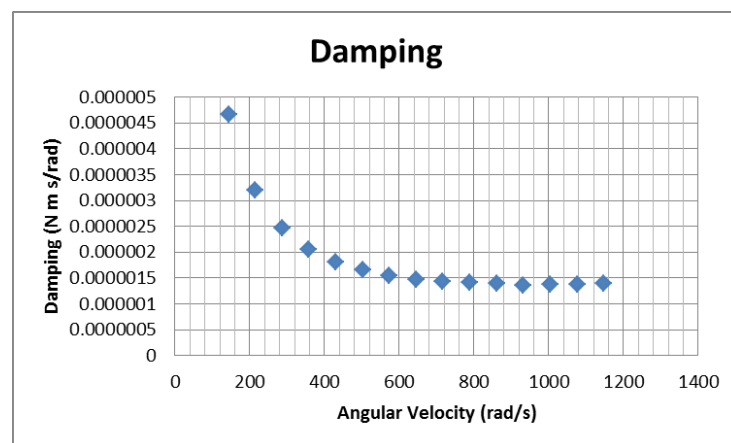


Figure 4.26. Damping vs. angular velocity in 2-16 V range

The graph clearly shows the behavior of damping and the steady state value can be found clearly. A curve fitting is applied in power form $b = A\omega^B + b_{ss}$ and it is given below.

$$b = 0.0412\omega^{-1.894} + 1.39 * 10^{-6} \quad (4.85)$$

The damping is relatively high at low angular velocities but it reaches a constant value after $600 \frac{\text{rad}}{\text{s}}$ which corresponds to nearly 8.4 volts applied to the motor and can be taken as $1.39 * 10^{-6} \frac{\text{Nms}}{\text{rad}}$. Also it is seen that the highest damping observed is $4.67 * 10^{-6} \frac{\text{Nms}}{\text{rad}}$ which is a very small value and can be neglected if needed.

4.5.4. Inertia

In order to find the inertia J of the DC motor, a rope with a known weight attached is rolled around the shaft of the DC motor. The duration of the fall of the weight is directly related to the inertia of the motor. Therefore, measuring the time of fall over a specified height enables calculation of the inertia.

The setup is shown in Figure 4.27. as a diagram. As seen from the figure, r is the shaft radius of the DC is motor and m is the weight on the rope. The stacking effect while winding the rope on the shaft is neglected.

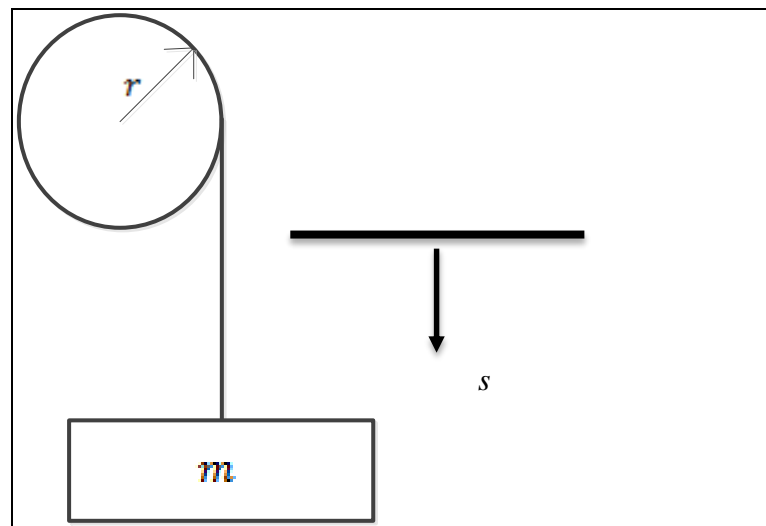


Figure 4.27. Diagram of the inertia experiment system

To solve for inertia of the DC motor free-body diagrams (FBD) the shaft and the weight are drawn using the model above (Figure 4.28).

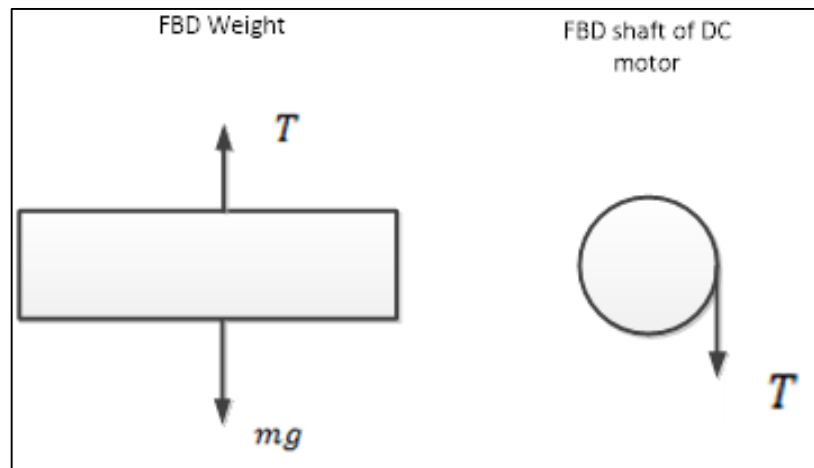


Figure 4.28. Free-body diagrams (FBD) for motor inertia testing setup.

The equations of motion are derived using the FBD as presented below.

$$J\dot{\omega} = Tr \quad (4.86)$$

$$ma = mg - T \quad (4.87)$$

It is seen here that the damping is neglected for ease of calculations since it can be considered to be negligible, as discussed before in Section 4.5.3 on damping. By combining the two equations by eliminating the tension term T the following first order differential equation is obtained.

$$J\dot{\omega} + rma = rmg \quad (4.88)$$

Since the rope is continuously tight and assumed to be inelastic, the relationship between angular acceleration and the acceleration of the weight is $\dot{\omega} = \frac{a}{r}$. Using this relationship the above equation changes to the form below.

$$\left(\frac{J}{r} + rm\right)a = rmg \quad (4.89)$$

The acceleration is then found as

$$a = \frac{mg}{\left(\frac{J}{r^2} + m\right)} \quad (4.90)$$

It is seen that acceleration is constant. Therefore, the position of the weight as a function of time is given by

$$s = s_0 + v_0 t + \frac{1}{2} a t^2 \quad (4.91)$$

where s_0 and v_0 are the initial height and the initial velocity. In this experiment, both of these initial values are taken as zero due to the selected coordinate system and initial condition. Therefore, $s = \frac{1}{2} a t^2$. Using the acceleration result, the equation below, relating height to time, is obtained.

$$h = \frac{1}{2} \frac{mg}{\left(\frac{J}{r^2} + m\right)} t^2 \quad (4.92)$$

Solving for inertia, we reach

$$J = \left(\frac{mgt^2}{2h} - m\right) r^2 \quad (4.93)$$

In the experiment, the motor is fixed at a point which is less than the rope length so that it is guaranteed that the weight will hit the ground. The weight is then released from rest and the time it takes to reach the ground is measured via a chronometer. The setup can be seen in Figure 4.29.

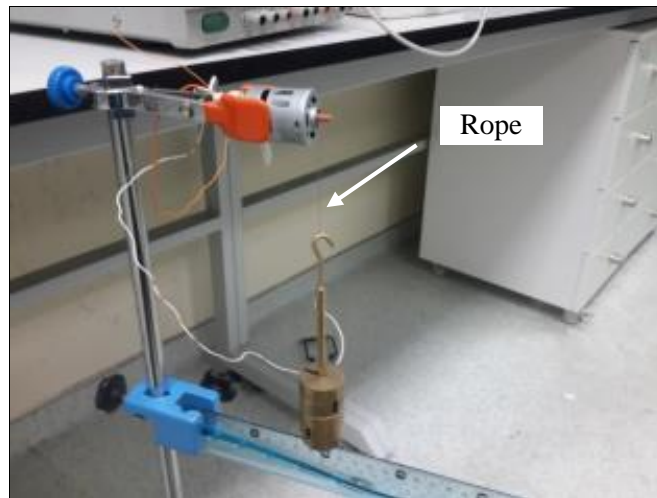


Figure 4.29. The DC motor, and, a rope with weight attached

It is important that the initial position of the weight is not too small and the weight itself is just enough to start the motion when it is released. This is necessary to decrease the human error in measuring time of motion.

The measured values for initial height, weight, and shaft radius are given in Table 4.8.

Table 4.8. Initial height, weight and shaft radius values used

Weight m(kg)	0.25
Initial height s(m)	0.705
Shaft radius r(m)	0.0012

After numerous trials, the experimental results yielded an average time of motion as 0.69 seconds. Plugging in the value measured for time and the other parameters the mass moment of inertia is obtained as

$$J = 8.32 * 10^{-7} \text{ kgm}^2$$

4.5.5. Inductance

For the measurement of inductance L an LCR meter is used. The LCR meter is connected to the terminals of the DC motor and the inductance value is found as given below.

$$L = 13.73 \text{ mH}$$

To verify this, an experimental setup is made where a power supply which is used as a constant voltage source, a shunt resistor and the DC motor are connected in series. The shaft of the DC motor is fixed thus it cannot rotate. This results in a simple RL circuit. The circuit diagram is shown in Figure 4.30. R_s is the shunt resistor and it is taken as $R_s = 23.37 \Omega$.

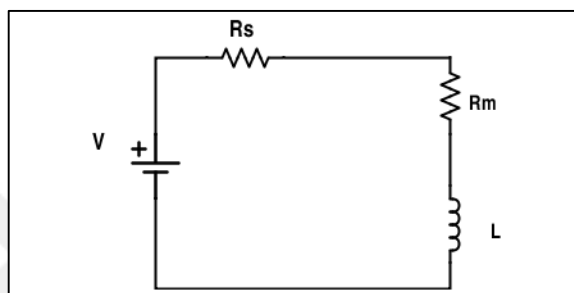


Figure 4.30. Circuit diagram of the experiment

A constant voltage V is applied as a step input to the system and the voltage change at the shunt resistor is measured. From this the current flow through the circuit is calculated using Ohm's law.

$$i = \frac{V_s}{R_s} \quad (4.94)$$

The total resistance of the system which is given below is calculated using Ohm's law after steady state has been reached;

$$R_{tot} = R_s + R_m + R_{supply} \quad (4.95)$$

$$R_{tot} = \frac{V}{i} \quad (4.96)$$

This is done in order to include the internal resistance of the power supply into the calculations.

The differential equation representing this system is given below.

$$L \frac{di}{dt} + (R_{tot})i = V \quad (4.97)$$

The solution of this differential equation is given below where the initial condition for current is taken as zero.

$$i = \frac{V}{R_{tot}} \left(1 - e^{-\left(\frac{R_{tot}}{L}\right)t} \right) \quad (4.98)$$

The current calculated using the shunt resistor and the theoretical current calculated using the above equation is plotted and compared.

The experiments are done using two different power supplies and a 9 V battery. Different voltages are applied to the system. The change in voltage does not affect the system behavior and the only affect is the change in steady state value of the system thus it is not necessary to conduct experiments using the same applied voltage.

First, a voltage of 10 V is applied to the system using the YH-305D model TT T-ECHI-C power supply (Power Supply 1). After steady state has been reached the total resistance of the system is calculated. This was found as given below;

$$R_{tot} = 52.21 \Omega$$

Since the shunt resistor is known and the motor resistance has been measured previously the resistance contributed by the power supply can be found as;

$$R_{supply} = 7.94 \Omega$$

Since all the variables in the theoretical calculation for current in Equation 4.98 is known the experimental result for current and the calculated theoretical result is plotted together in a graph which is given in Figure 4.31.

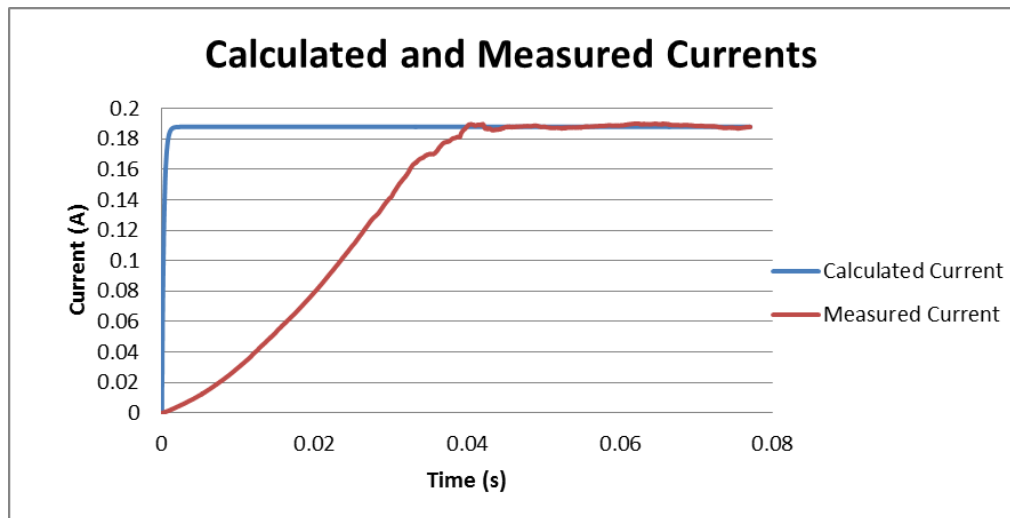


Figure 4.31. Response of the motor internal circuit to a step input (Power Supply 1).

It is seen that there is a large difference between the two curves in transient stage. This is due to the effect of the power supply. The power supply contains a large control mechanism to regulate current and because of this it is not able to supply a voltage as a step input to the circuit and thus it creates a lag in supplied voltage.

Another test is done using a different power supply, FeedBack Power Supply 01-100 (Power Supply 2). The supply voltage was 5 V. The total resistance is calculated using the steady state current and it is found as;

$$R_{tot} = 46.11 \Omega$$

The resistance of the power supply was found as;

$$R_{supply} = 0.84 \Omega$$

The experimental result for current and the calculated theoretical results are plotted together as given in Figure 4.32. In this graph it is seen that the difference between the curves are lower. This is due to the power supply being better at providing a step input to the circuit.

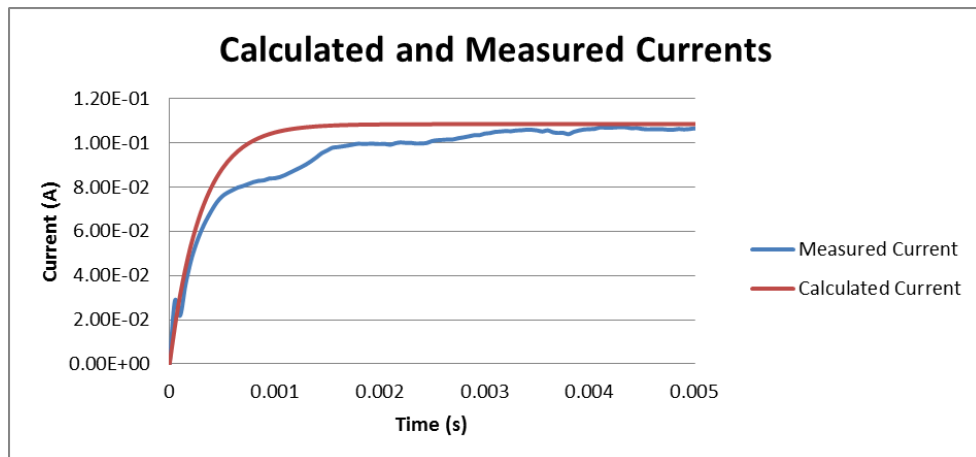


Figure 4.32. Response of the motor internal circuit to a step input (Power Supply 2).

In order to rule out the effects of the control mechanism problem in the power supplies, a 9 V battery is used as a constant voltage source. The total resistance is measured as;

$$R_{tot} = 65.05 \Omega$$

The resistance of the power supply was found as;

$$R_{supply} = 19.78 \Omega$$

The experimental result for current and the calculated theoretical results are plotted together as given in Figure 4.33.

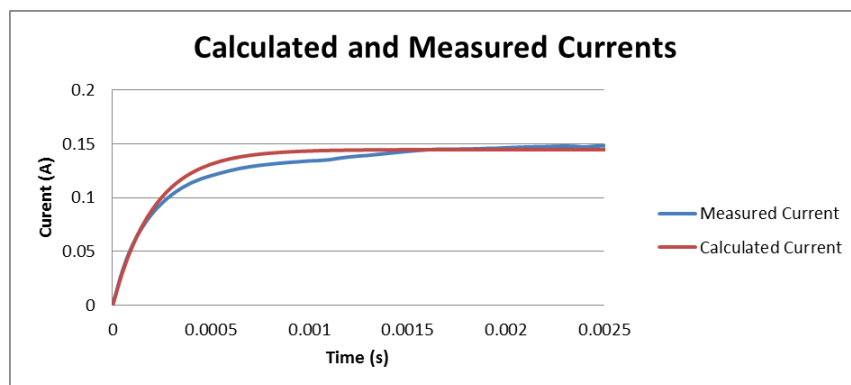


Figure 4.33. Response of the motor internal circuit to a step input using 9V battery.

It is seen that there is no lag in the system since there is no control mechanism regulating the current thus the calculated and the measured current values are nearly the same.

This proves the inductance value obtained from the LCR meter is valid. The 9 V battery results show that the power supplies used are not able to provide a correct step input voltage to the system due to their control mechanisms.

4.6. CONTACT/IMPACT PROBLEM MODELING

It is seen from the design that there are three points where contact problems occur. These contact problems are between the tip of the conical spring and the tire (contact and no-contact states of the tip); the pulley and the tip of the conical spring (tightness and looseness of the rope); and, the ratchet and the pulley shaft (engaged or disengaged states of the ratchet).

4.6.1. Tip Of The Conical Spring And Base

In this section, the contact between the tip of the conical spring and the tire is modeled.

Firstly, a condition representing the contact between the tip of the conical spring and the point on the tire should be defined. The position of the contact point on the tire is denoted as D , which was modeled in Section 4.2 and the position of the tip of the conical spring is denoted as p_c , which is measured from the undeflected position of the tire. This is shown in Figure 4.34.

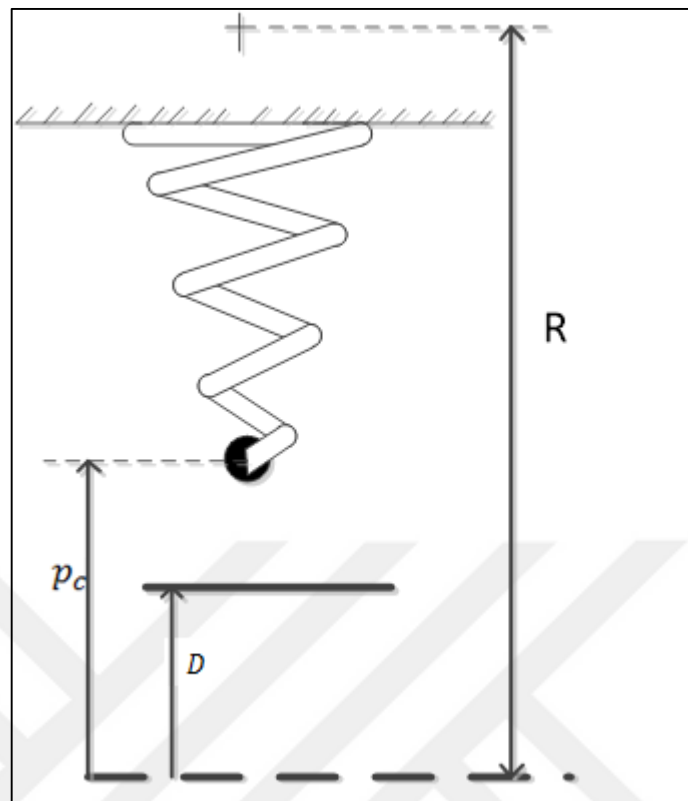


Figure 4.34. Positions of tire and spring as measured from the undeflected tire position.

The condition is given as shown below.

$$D = p_c \quad (4.99)$$

It is known that the position of the tip of the spring can only be greater or equal to the position of the deflection of the tire. This can be said by assuming no penetration occurs between the two parts.

If $p_c > D$, then the conical spring is not in contact with the tire. Thus, if there is no contact between the two parts and a state of contact is detected, an impact occurs where momentum equations must be solved to find the kinematics after the impact. In this, the coefficient of restitution between the tire surface and the tip of the conical spring is used as shown below.

$$e_{tire} = \frac{(\dot{p}_c - D_v)_{after}}{(\dot{p}_c - D_v)_{before}} \quad (4.100)$$

4.6.2. Rope Tightness

Similar boundary condition must be defined for the pulley and the tip of the conical spring since the connection is done by a rope. The rope can have two states which are *tight* and *loose*. The state of the rope is determined by the condition given below where the static equilibrium positions of the pulley θ_{ps} and the tip of the conical spring p_{cs} found in Section 4.1 are used.

$$(p_c - p_{cs})r_p = (\theta_{ps} - \theta_p) \quad (4.101)$$

The loose case is defined as shown below;

$$(p_c - p_{cs})r_p > (\theta_{ps} - \theta_p) \quad (4.102)$$

This means that the tip of the conical spring has travelled a greater distance than the pulley has wound up the rope, thus the rope becomes loose.

The impact in this case is defined as the rope changing states from loose to tight. Since the rope cannot exert a negative tensile force to a connected body there is no collision from changing states from tight to loose.

To calculate the kinematics after the collision, the momentum equation must be solved. While doing this the rope is assumed to be fully elastic thus momentum is conserved. This equation is given below;

$$m_{eq}r_p^2\dot{p}_{c_{before}} + (I_p + I_s)\dot{\theta}_{p_{before}} = m_{eq}r_p^2\dot{p}_{c_{after}} + (I_p + I_s)\dot{\theta}_{p_{after}} \quad (4.103)$$

It is seen that there are two unknowns in the above equation. These are the angular velocity of the pulley and the velocity of the tip of the conical spring after the collision. In order to

solve this problem another equation is needed. This second equation comes from the conservation of energy. This is given below;

$$\frac{1}{2} m_{eq} \dot{p}_{c_{before}}^2 + \frac{1}{2} (I_p + I_s) \dot{\theta}_{p_{before}}^2 = \frac{1}{2} m_{eq} \dot{p}_{c_{after}}^2 + \frac{1}{2} (I_p + I_s) \dot{\theta}_{p_{after}}^2 \quad (4.104)$$

Solving these equations together the angular velocity of the pulley and the velocity of the tip of the conical spring after the collision are obtained as given below;

$$\dot{p}_{c_{after}} = \frac{(k-1)}{(k+1)} \dot{p}_{c_{before}} - \frac{2r_p}{k+1} \dot{\theta}_{p_{before}} \quad (4.105)$$

$$\dot{\theta}_{p_{after}} = \frac{(1-k)}{(k+1)} \dot{\theta}_{p_{before}} - \frac{2k}{r_p(k+1)} \dot{p}_{c_{before}} \quad (4.106)$$

4.6.3. Ratchet Engagement

The ratchet in this design is driven by the shaft connected to the pulley and the driven part connected to the ratchet is the generator. The driver shaft is connected to the inner ring and the outer ring is connected to the driven generator shaft. This is shown in Figure 4.35.

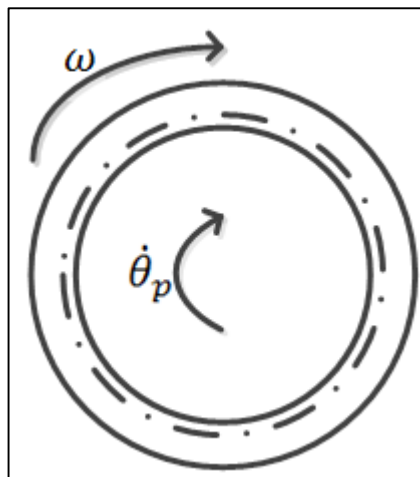


Figure 4.35. Driving and driven angular velocities

The condition for the ratchet to be engaged is given as

$$\dot{\theta}_p = \omega \quad (4.107)$$

It is known that the angular velocity of the load cannot be lower than the angular velocity of the ratchet.

There are two conditions for the ratchet to be disengaged these are given in below;

$$\dot{\theta}_p \leq 0 \quad (4.108)$$

or

$$\dot{\theta}_p > 0 \text{ and } \ddot{\theta}_p < \dot{\omega} \quad (4.109)$$

The case for engagement or disengagement is permanent until the other condition is satisfied.

The assumption is made that when the ratchet changes state from being disengaged to being engaged, the pulley and the shaft energy is very large that it can be treated as an infinite energy source. Thus the velocity of the pulley is not affected by the transfer of rotational energy via the ratchet to the generator. The collision analysis is not done for the ratchet.

5. NUMERICAL SIMULATION

Numerical simulation codes were written in order to simulate the system. The dynamic models provided in Section 2 are used to generate these simulation codes.

5.1. CONTACT AND COLLISION PROBLEM SIMULATION

In this simulation the tip of the conical spring can lose contact with the tire base and the rope in the pulley can get to a loose state.

The simulation determines the state changes and calculates impact problems for the tip of the conical spring and the pulley. These calculations are done using the methods provided in section 2.6.

The flow chart of the algorithm of this numerical simulation code is given in Figure 5.1.

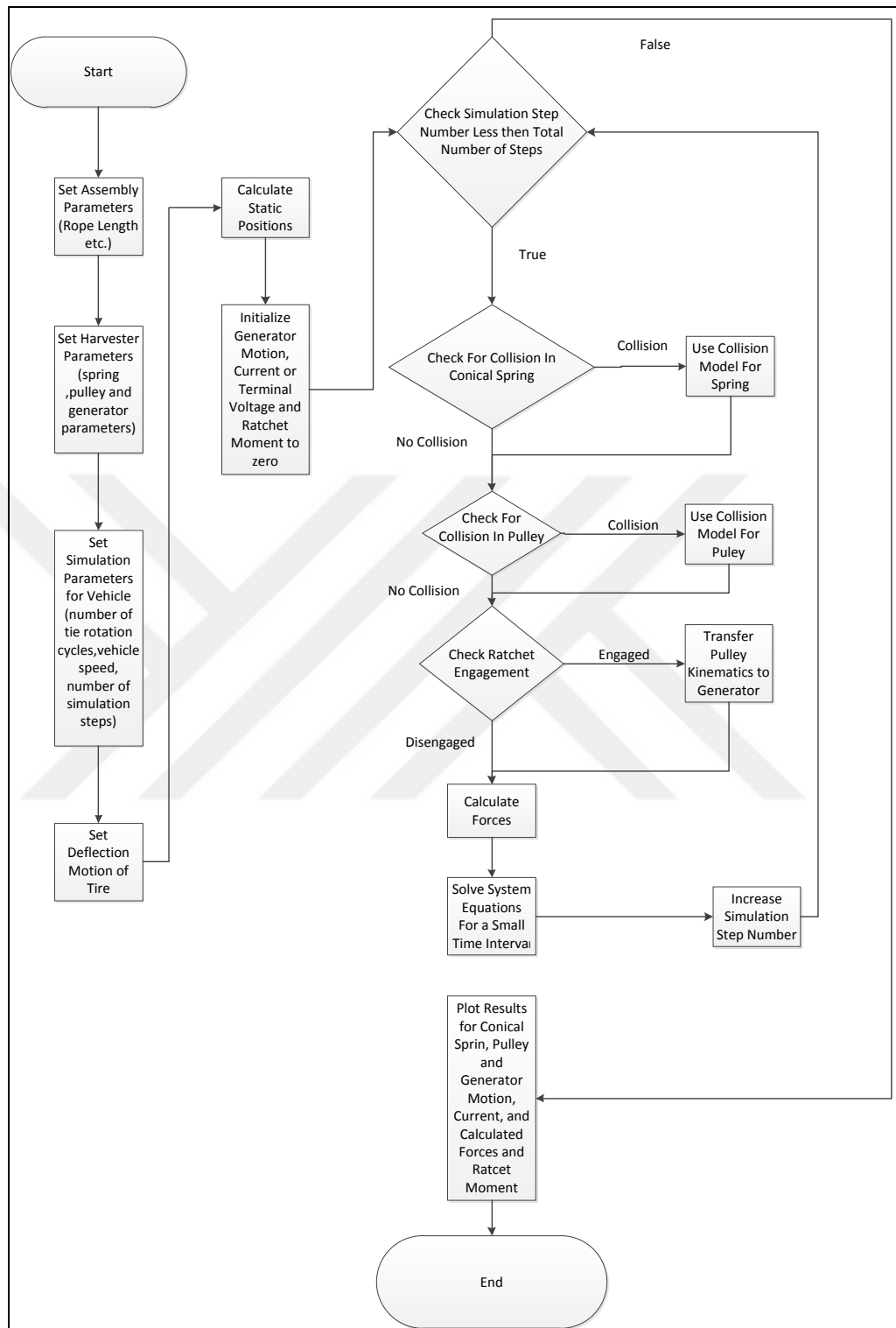


Figure 5.1. Flowchart of Contact and Collision Problem Simulation

5.2. COMPLETE POWER TRANSMISSION TO PULLEY

An assumption is made that the contact between the ground and the tip of the conical spring is constantly maintained and the rope is always tight. Thus, the deflection motion of the tire is directly converted to angular motion of the pulley. Thus, it can be said that the power is completely transmitted to the pulley.

After this transmission is done the ratchet state is checked since all the kinematic properties of the pulley are known. The appropriate generator model is used for open or closed circuits, and, according to the ratchet state the generator dynamic equations are solved for the ratchet velocity, acceleration, current, and the rate of change of current. The flow chart of the algorithm of this numerical simulation code is given in Figure 5.2.

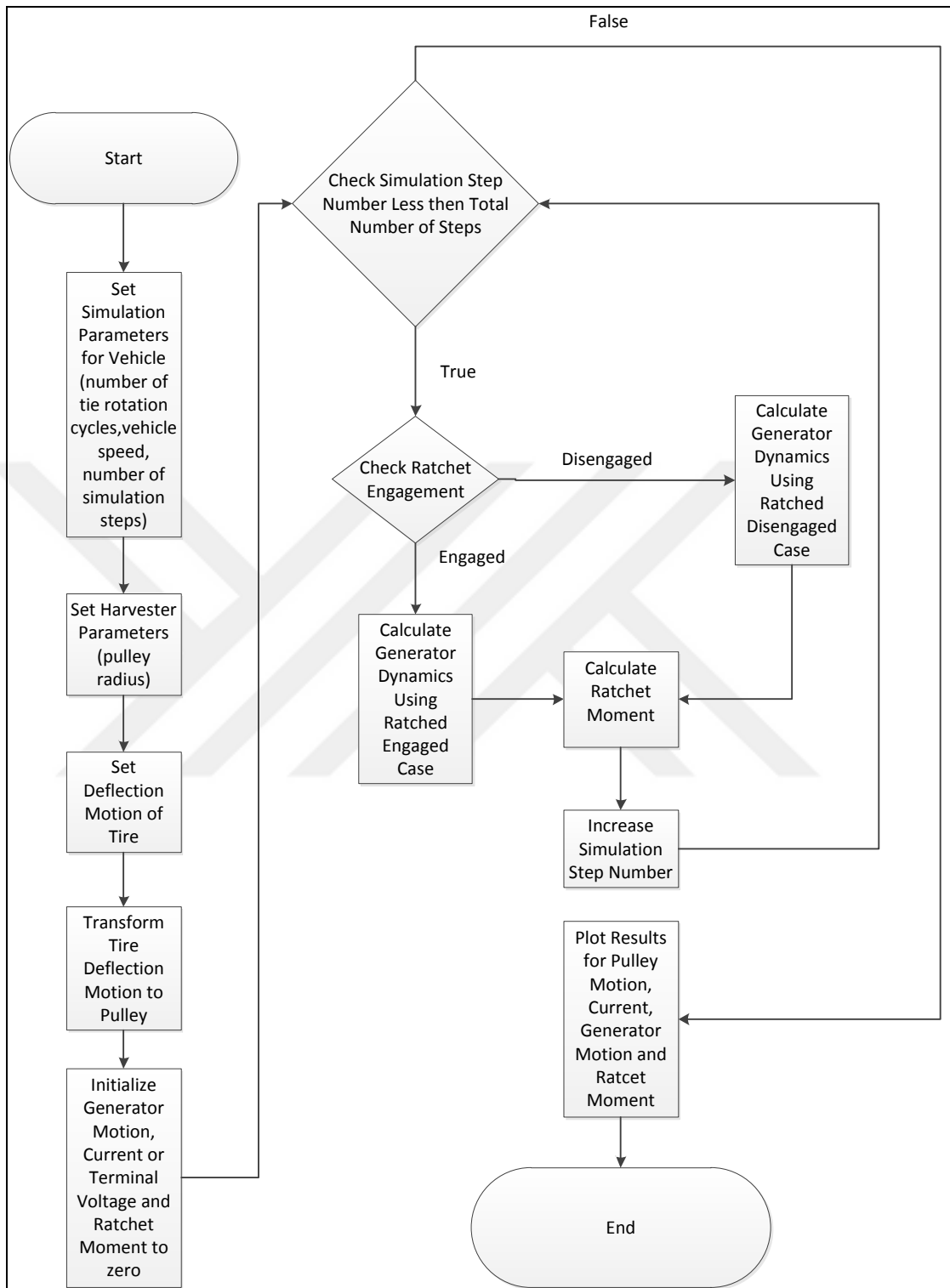


Figure 5.2. Flowchart of complete power transmission to pulley simulation case

6. EXPERIMENTAL DESIGN AND TESTING

An experimental setup is designed in order to test the TPMS energy harvester. This test is necessary in order to validate the numerical simulations performed using the previous algorithms provided in Section 5.

The experimental setup consists of two parts. The first part includes a design of a cam in order to simulate the tire deflection and the second part is the prototype energy harvester itself.

6.1. CAM DESIGN AND MECHANISM

A cam is designed to provide the radial deflection model, which is modeled in Section 4.2. A roller is placed inside the cam and the radial change in diameter provides the modeled deflection. The cam profile is given in Figure 6.1.

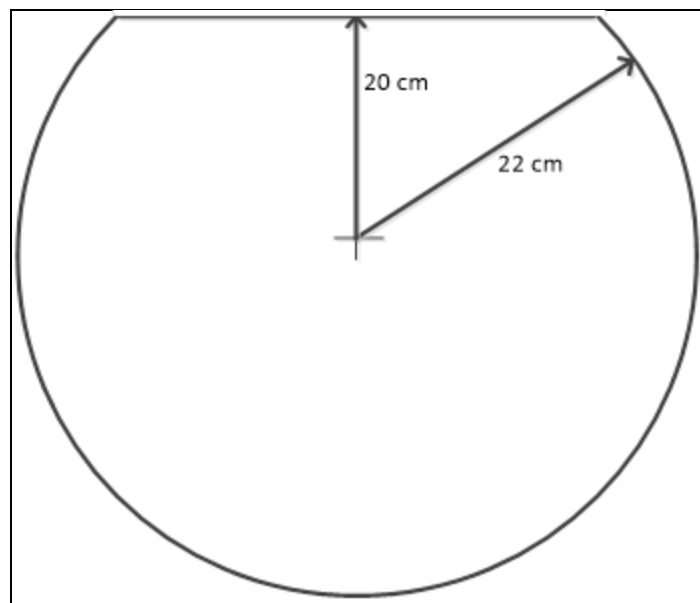


Figure 6.1. Basic sketch of the designed cam

This cam profile is obtained by placing a bar inside a tire rim. This is shown in Figure 6.2.



Figure 6.2. Cam obtained by placing a bar inside a circular part

Due to manufacturing errors the steel bar placed in the circular part is not straight. This causes a change in the radial deflection profile. This issue is not taken into account.

This produced cam is placed on a shaft. The shaft contains a gear that is used to connect to a DC motor in order to drive the cam. The gear ratio used is 3:1 in order to increase the torque produced by the driving DC motor on the cam. The shaft is then placed on a structure in order to hold the cam and the DC motor in place. This is shown in Figure 6.3. Figure 6.4. shows the individual components in detail.



Figure 6.3. Structure where the DC motor and the Cam is placed

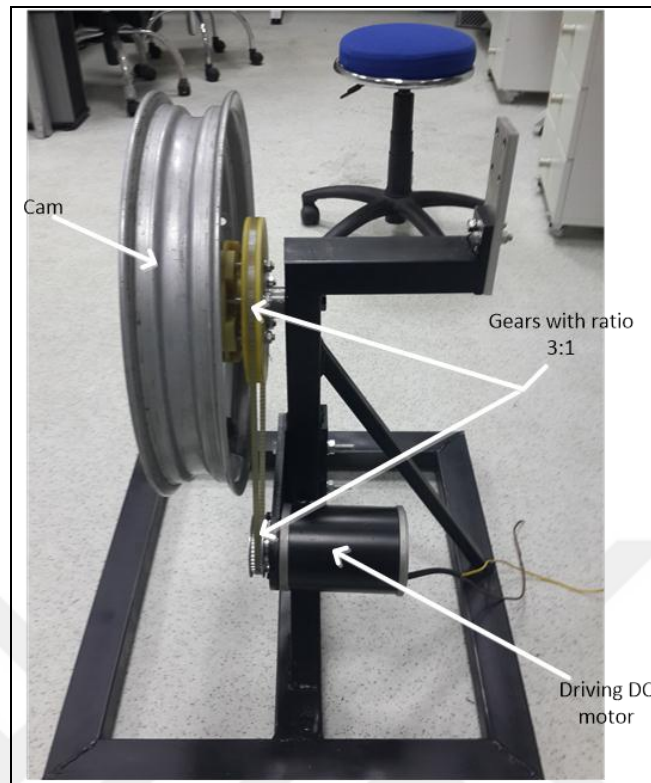


Figure 6.4. Components of the main structure

6.2. PROTOTYPE DESIGN GENERATION ONE

A scaled up version of the prototype is designed for experimental testing. This prototype is shown in Figure 6.5. Figure 6.6 shows the components in detail.

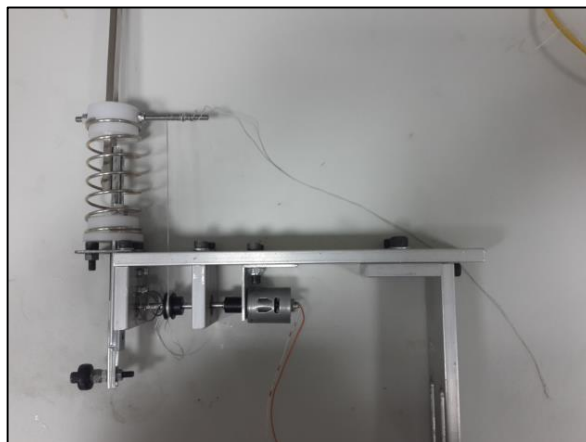


Figure 6.5. Prototype generation One

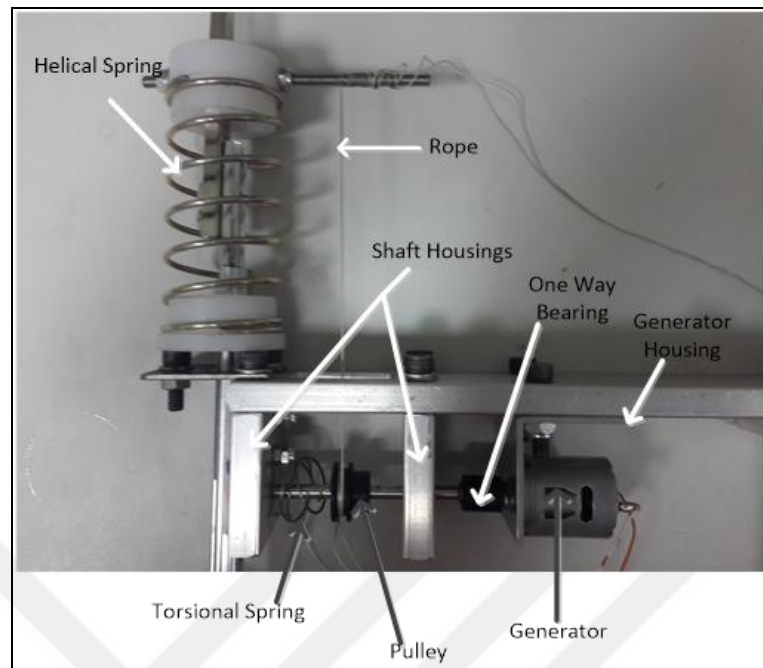


Figure 6.6. Components of the prototype generation one

Here a helical spring is used where a conical spring is supposed to be in the original design. However, the only reason for using a conical spring in the original design is to prevent damage to the tire in case of flat tire, which would be a possibility had a straight helical spring been used due to the nonzero solid height. Therefore, use of a helical spring in place of a conical spring will not affect the function of the harvester. The properties of the helical spring used in the experiment are given in Table 6.1.

Table 6.1. Helical spring properties used in the prototype

Major Diameter	40 mm
Height	113 mm
Wire Thickness	2.5 mm
Number of Coils	8
Material	stainless steel 17-7 a313
End Type	Closed Ends

The stiffness of the helical spring is calculated using Equation 3.6 as $1.168 \frac{N}{mm}$.

The torsional spring used in the experimental setup is basically another conical spring. This however causes problems in high angular rotations. No calculations for the stiffness of the torsional spring is made due to it being used only for testing purposes. As a one way bearing, OWC307GXLZ is used from BOCA company.

The prototype is placed on the main structure where the cam is placed. This is shown in Figure 6.7.



Figure 6.7. Prototype placed on the main structure of the cam

This experimental setup is tested in order to check if it works properly. A voltage of 3 V is applied to the driving DC motor in order to rotate the cam and the voltage between the terminals of the generator are measured. The test results are as shown in Figure 6.8.

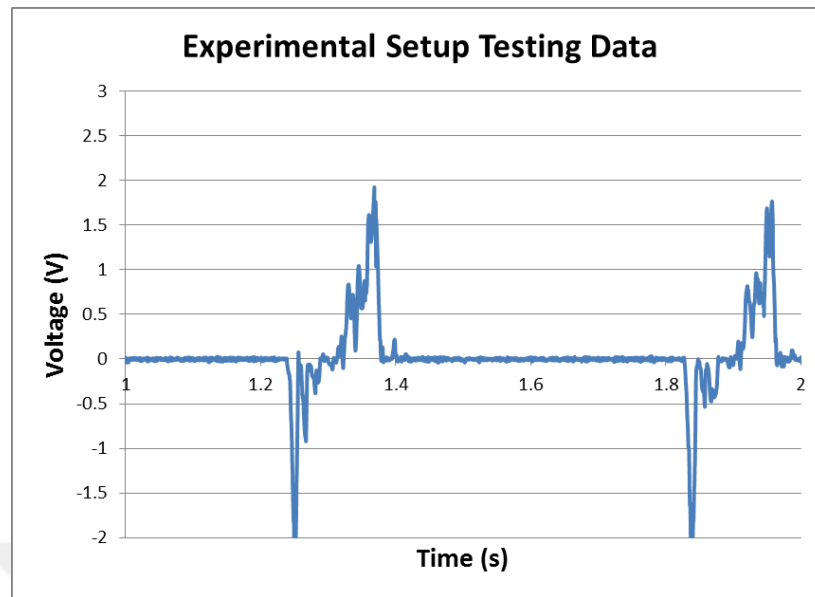


Figure 6.8. Prototype test results

Here it is seen that the one way bearing is not operating correctly because it is engaged all the time since negative voltage peaks are obtained. This is thought to be by the coupling element that the one way bearing is placed in and unwanted loads are accumulated on the one way bearing. Due to the problems in the torsional spring and the one way bearing some changes are made to the prototype design.

6.3. PROTOTYPE DESIGN GENERATION TWO

In order to tackle the problems observed in the generation one design. Some changes are made. In order to reduce the unwanted loads on the one way bearing a 3 mm helical coupling shown in Figure 6.9. is used.



Figure 6.9. Helical coupling used to relieve the unwanted loads on the bearing

Turning is used to expand the 3mm shaft hole of the coupling in one side in order to place the one way bearing inside the coupling. The prototype with the coupling used is shown in Figure 6.10.



Figure 6.10. The prototype with the helical coupling and new torsional spring.

As a torsional spring a helical spring is used. The geometric properties of this spring are given in Table 6.2.

Table 6.2. The properties of the helical spring used in place of the torsional spring.

Major Diameter	17 mm
Wire Thickness	1 mm
Number of Coils	4.25
End Type	Straight Offset

The material for the helical spring is unknown here. To determine the material of the helical spring an experiment was conducted. The spring was placed in an Instron universal testing machine. A compressive deflection was given to the spring and the force was measured using the sensors in the universal testing machine. The graph of the experimental results is given in Figure 6.11.

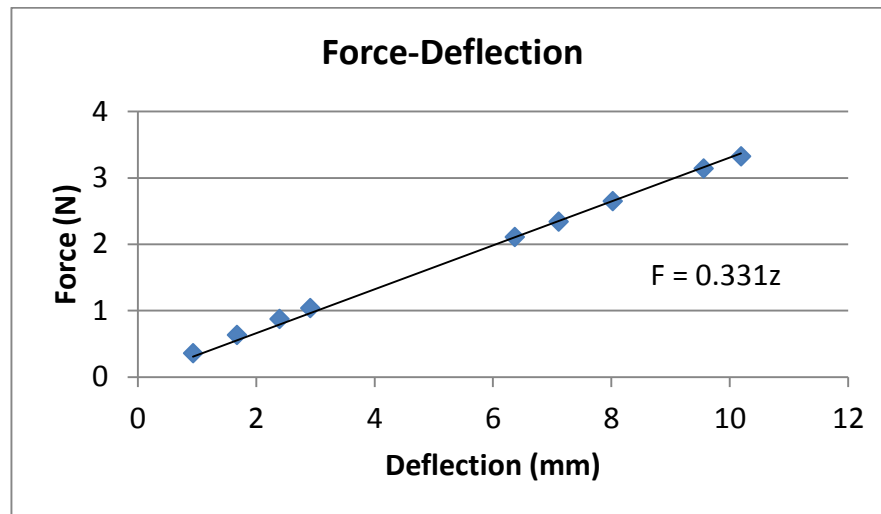


Figure 6.11. Deflection and force data obtained from universal testing machine

Using the slope of the graph the linear spring constant is obtained as $0.331 \frac{\text{N}}{\text{mm}}$. The spring constant is used to calculate the shear modulus of the material. The shear modulus is obtained as 52 GPa . In the widely used spring materials the property closest to this shear modulus is Beryllium-copper B197 with shear modulus of 50.3 GPa . Thus the material of the torsional spring is determined as Beryllium-copper B197. As a result, the torsional stiffness of the helical spring is calculated as $0.0283 \frac{\text{Nm}}{\text{rad}}$.

This new prototype is tested in order to check if it works properly. A voltage of 3 V is applied to the driving DC motor in order to rotate the cam and the voltage between the terminals of the generator is measured. The test results are as shown in Figure 6.12.

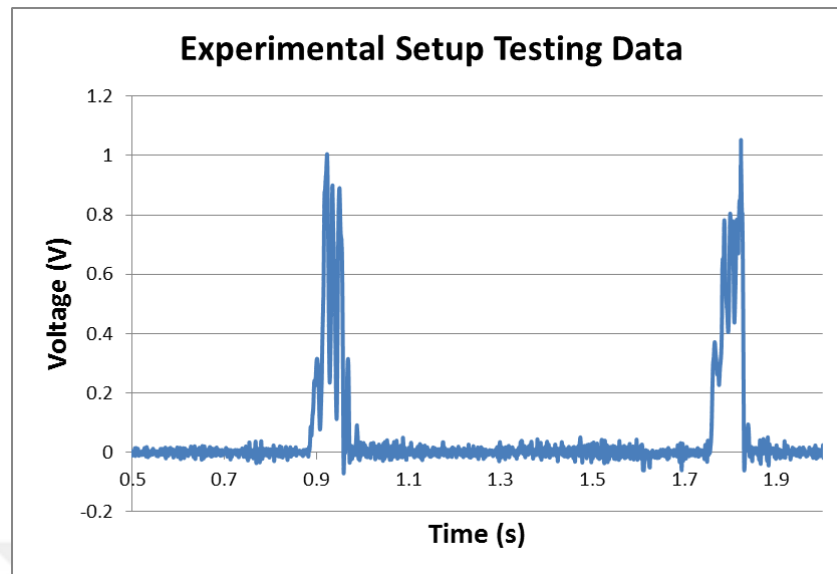


Figure 6.12. Prototype test results

Since the results obtained from the new system are as expected, one can claim that the one way bearing is operating better.

6.4. EXPERIMENTAL PROCEDURE

6.4.1. Measuring the Voltage Generated

A voltage source is connected to the DC motor in order to rotate the cam. After the cam has reached its full speed, data of the voltage generated between the terminals of the generator is measured. This is done by using a data acquisition card (DAQ) card and LABVIEW software of National Instruments Company.

6.4.2. Measuring Power Output

The generator is connected to a circuit containing two parallel resistors, acting as an adjustable electrical load. This circuit diagram is shown in Figure 6.13.

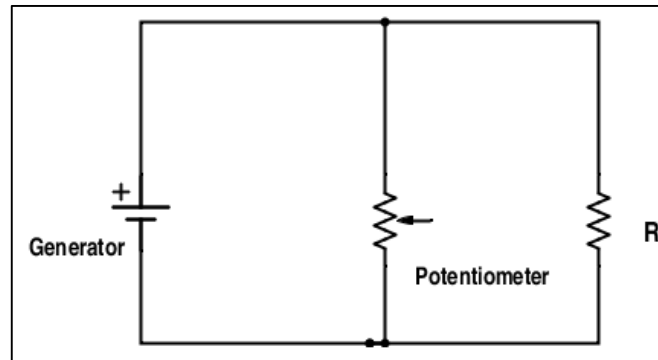


Figure 6.13. Diagram of the circuit in order to measure power output over the resistor

This is done using a 500 ohm potentiometer and a 125 ohm resistor. This circuit is done in order to scale the equivalent resistance to a range of 0-100 ohms. The voltage difference between the terminals of the dc motor is measured and the current is calculated using Ohm's law given below.

$$i = \frac{V}{R_{eq}} \quad (6.1)$$

where R_{eq} is the equivalent resistance of the circuit and it is measured before starting the experiment.

The electrical power formula given below is used in order to calculate the power output of the generator.

$$Power = i^2 R_{eq} = \frac{V^2}{R_{eq}} \quad (6.2)$$

7. RESULTS AND DISCUSSION

7.1. OPEN CURCUIT EXPERIMENTS

A voltage of 3 V is applied to the DC motor and the open circuit voltage is measured between the terminals of the generator. The results are given in Figure 7.1.

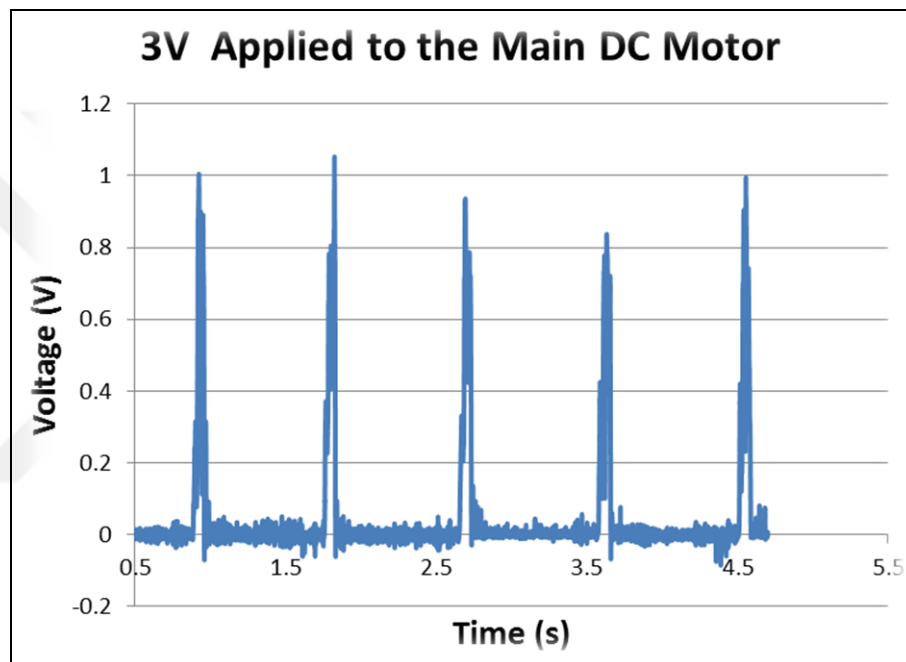


Figure 7.1. Voltage generated by applying 3V to the main DC motor

The voltage profile is observed to be periodic with a period of 0.89 seconds, which is same as the period of the cam rotation. This period corresponds to a vehicle speed of 5 km/h. The mean peak voltage is measured as 0.95 V and the RMS voltage generated is found as 0.17 V.

The same experiment was done using the numerical simulation algorithm presented in Section 5.2 using the period found from the experiment. The numerical simulation results are given in Figure 7.2.

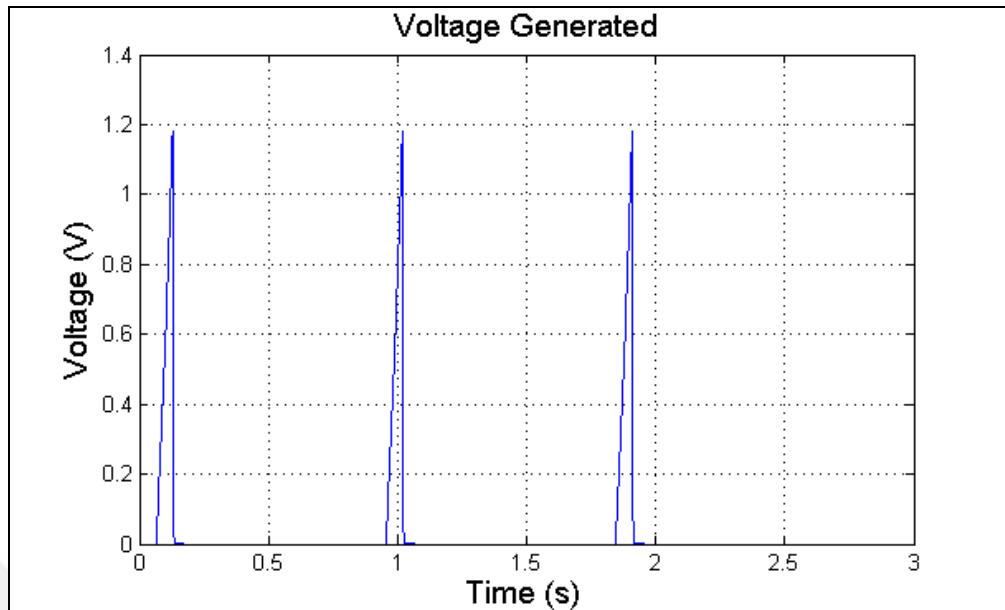


Figure 7.2. Numerical simulation results for tire period of 0.89 seconds

The peak voltage generated from the simulation is 1.18 V and the RMS voltage generated is found as 0.17 V. These results are summarized in the following table (Table 7.1).

Table 7.1. Summary of the results obtained from applying 3 V to the main DC motor

Method	Peak Open circuit Voltage (V)	RMS Open circuit Voltage (V)
Experiment	0.95	0.17
Numerical Simulation	1.18	0.17
% Deviation	24.21	0.00

It is seen from both numerical and experimental results are considerably close to one another where the deviation of the peak open circuit voltage is 24.21% and the deviation of RMS voltage is 0.00% which means that although the signals may not be the same they are acceptable. The same experiment and numerical simulation is done when 4 volts are applied to the DC motor rotating the cam in order to verify the numerical simulation algorithm again. The experimental results are given in Figure 7.3.

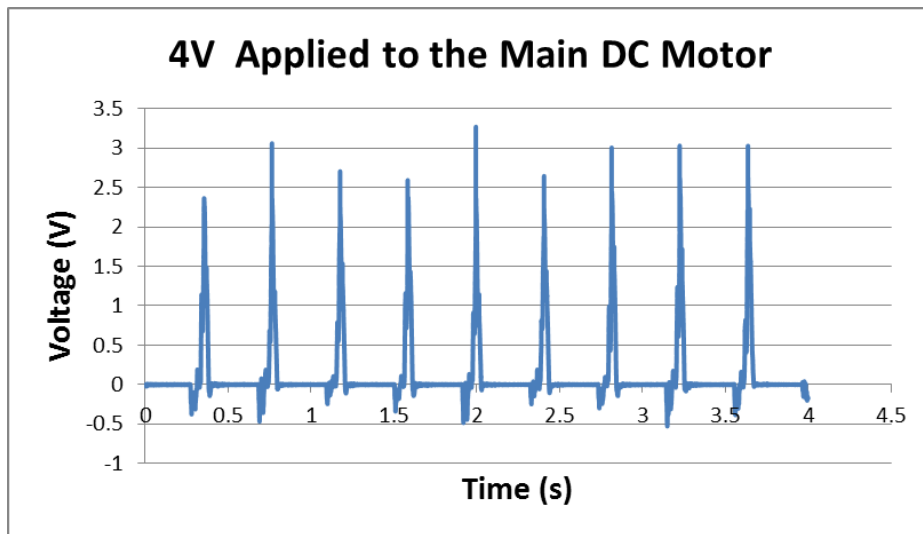


Figure 7.3. Voltage generated by applying 4V to the main DC motor

The voltage profile is observed to be periodic again and the period of the voltage is measured from the graph as 0.41 seconds which is same as the period of the cam rotation. This period corresponds to 11 km/h vehicle speed. The mean peak voltage is calculated as 2.72 volts and the RMS voltage generated is found as 0.43 volts.

The same experiment was done using the numerical simulation algorithm in Section 5.2 for open circuit voltage using the period found from the experiment. The numerical simulation results are given in Figure 7.4.

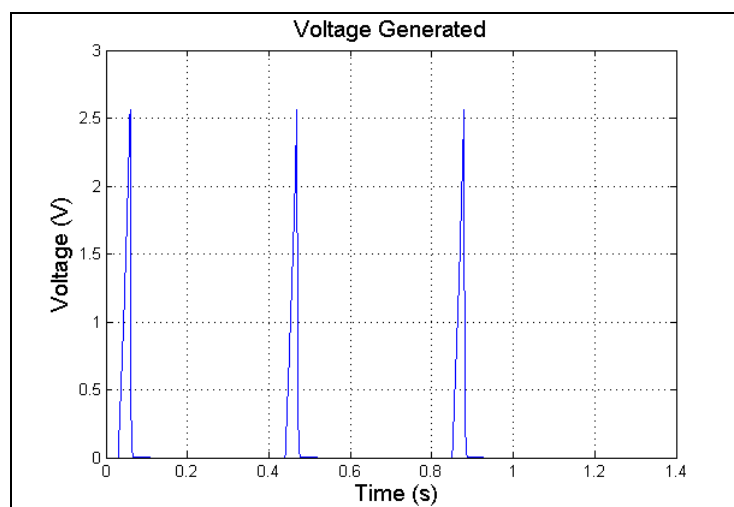


Figure 7.4. Numerical simulation results for tire period of 0.41 seconds

The peak voltage generated from the simulation is 2.62 volts and the RMS voltage generated is found as 0.39 volts. These results are summarized in the following table (Table 7.2).

Table 7.2. Summary of the results obtained from applying 4 V to the main DC motor

Method	Peak Open circuit Voltage (V)	RMS Open circuit Voltage (V)
Experiment	2.72	0.43
Numerical Simulation	2.62	0.39
% Deviation	-3.68	-9.3

The deviations of the numerical simulation have many sources, some of which are listed below.

- In the experiment the cam rapidly decelerates and accelerates when compressing the conical spring (this effects the voltage peak values generated).
- The one way bearing does not work ideally since negative voltages are observed in the experiment.
- At slow speeds, when the tip of the helical spring is near the middle of the straight piece on the rim, the generator slows down and passes into the nonlinear damping zone.

In spite of these reasons, the results obtained from the experiments and numerical simulation can be said to be considerably close to one another. The deviations of 4 V experiments are -3.68% for peak voltage and -9.3% for RMS voltage which are acceptable. This indicates the validity of the analytical model and the numerical algorithm for open circuit case.

7.2. CLOSED CIRCUIT EXPERIMENTS

For the closed circuit experiments with an electrical load a voltage of 3 V is applied to the DC motor rotating the cam. Then, the equivalent resistance connected to the generator is set to values ranging from 4 Ω to 89 Ω . The power output is measured. The same experiment is done numerically for a resistance range of 0 Ω to 100 Ω . Maximum power

obtained for each resistance value is plotted for both experimental and numerical simulation. The results are given in Figure 7.5.

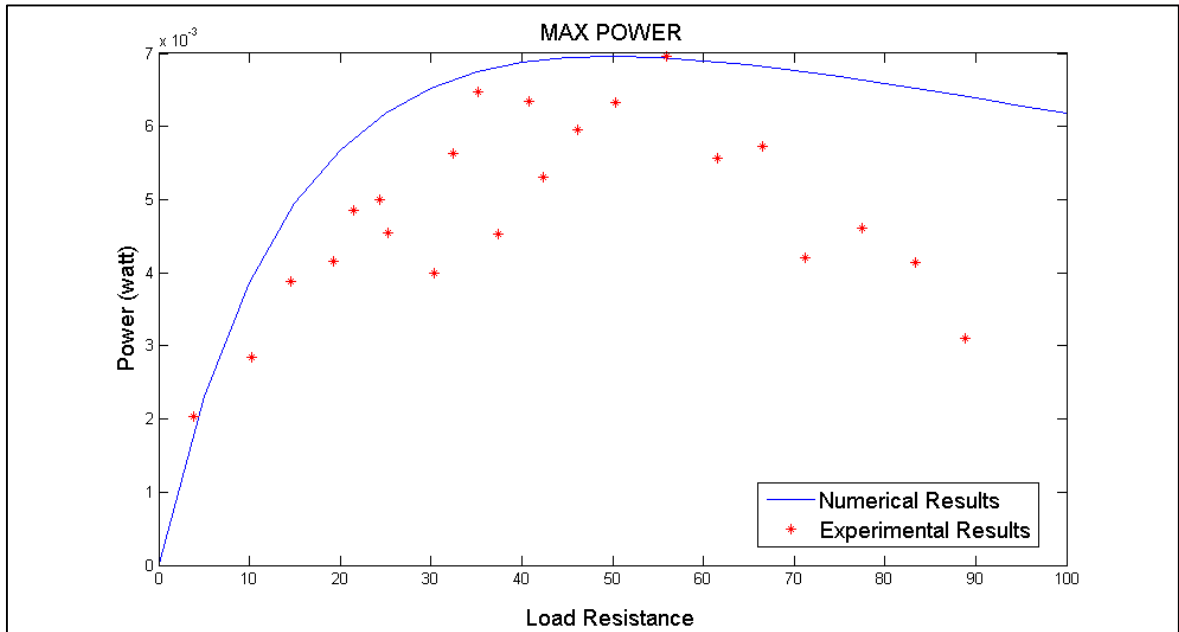


Figure 7.5. Maximum power obtained for experiment and numerical simulation

It is seen that the maximum points of the numerical simulation result and the experimental results match and it is seen that the maximum point of numerical simulation is obtained at 50 Ω. This is due to the generator internal resistance increase due to connection of cables and the connection to the circuit. Thus it can be said the maximum power output is obtained at the equivalent internal resistance of the generator.

In the right portion of the maximum point the results seem to diverge from one another, this is due to the heating of the resistors both in the circuit connected to the generator and the internal resistor of the generator.

Numerical simulation is done to obtain average power output for a vehicle velocity range of 0 to 150 km/h. The results are given in Figure 7.6.

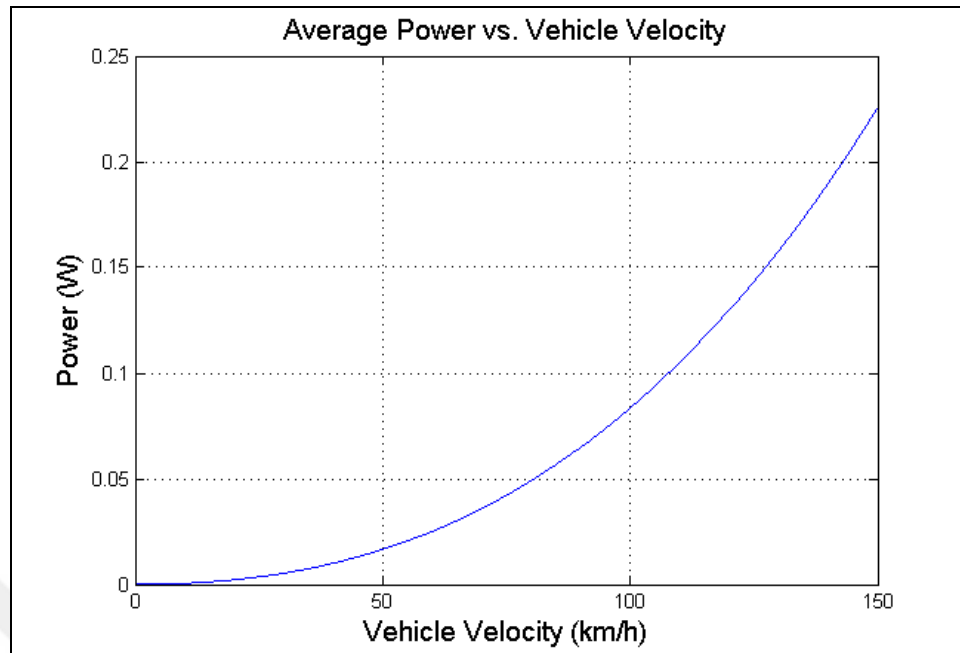


Figure 7.6. Average power simulation results vs. vehicle speed.

It is seen that the average power output behaves similarly to a second order polynomial. Thus a second order polynomial curve fitting is applied and the equation obtained is given below;

$$Power_{average} = 10^{-5}V^2 - 0.00003V$$

The correlation coefficient of the fit (goodness of fit) is 0.998. This strongly supports the choice a second order polynomial for the curve fit.

8. CONCLUSION AND FUTURE WORK

In this thesis a novel, patent-applied design is modeled. The modeling includes vehicle tire deflection modeling, conical spring equivalent mass modeling, modeling dynamical equations of systems and DC generator modeling and characterization. By using these models the numerical algorithms are generated and used to simulate the system under given vehicle velocities using the numerical software MATLAB. In order to compare the numerical algorithm validity prototype is designed. After the prototype is tested to work properly, open and closed circuit experiments are conducted.

The open circuit experiments are used to verify the validity of the numerical algorithm. The closed circuit experiments are one in order to measure the power output of the harvester under certain electrical loading conditions. The average power output curve is generated for vehicle velocity ranging from 0 to 150 km/h vehicle speed.

It is observed that the power output of the harvester is proportional to the square of the vehicle speed. At low vehicle speeds (around 20 km/h) the harvester generates an average power of 2.2 mW. This is enough power for a currently used TPMS to work properly.

As future work the algorithm solving for contact and collision problem can be perfected to solve the system behavior at high speeds when the system is working non-ideally (conical spring loses contact, rope loosens).

REFERENCES

1. Office of Regulatory Analysis and Evaluation, NHTSA. Tire Pressure Monitoring System. Report, 2005.
2. John Finneran. Tire Pressure Monitoring System Compliance Test Program. *SAE Government/Industry Meeting*, 2006.
3. Office of Regulatory Analysis and Evaluation, NHTSA. Proposed New Pneumatic Tires For Light Vehicles. Report, 2001.
4. Continental Trading, VDO, Continental Lastik Hava Basinci Izleme Sistemleri İçin Yedek Parçalar. Report, 2012
5. Wikipedia, “Direct TPMS”, https://en.wikipedia.org/wiki/Direct_TPMS [retrieved 1 July 2015]
6. B. Banazwski and R. K. Shah. The Role Of Fuel Cells For Consumer Electronic Products And Toys. *1st Int. Conf. on Fuel Cell Science, Engineering and Technology*, Rochester, NY, USA, 2003.
7. A. H. Epstein. Millimeter-Scale, Micro-Electro-Mechanical Systems Gas Turbine Engines. *Journal of Engineering. Gas Turbines Power*, 2004.
8. J. J. Kiely, D. V. Morgan, and D. M. Rowe. Low Cost Miniature Thermoelectric Generator. *Electronics Letters*, 1991.
9. H. A. Sodano, G. Park, D. J. Leo, and D. J. Inman. Model Of Piezoelectric Power Harvesting Beam. *ASME International Mechanical Engineering Congress*, 2003.

10. S. P. Beepy, R. N. Torah M. J. Tudor, P. Glynne-Jones, T. O'Donnell, C. R. Saha and S. Roy. A Micro Electromagnetic Generator For Vibration Energy Harvesting. *Journal of Micromechanics And Microengineering*, 2007.
11. S. H. Choi, D. P. Chun, D. H. Kwon, S. K. Kim, H. K. Na and W.J Lee. Power Supply Using Static Magnetic Field Of Tire Pressure Monitoring System. US7541916 B2, 2009.
12. B. L. Bircumshaw, J. F. Bryzek, E. A. Logan and C. A. Ray. Integrated Tire Pressure Sensor System. WO2007064961 A3, 2009.
13. S. Kumar, J. D. Cook, G. O'Briend, M. A. J. Qasimi, R. C. Sorneson, B. J. Marsh and V. V. Avramescu. Mechanical Packaging Of Surface Acoustic Wave Device For Sensing Applications. US7576470 B2, 2008.
14. T. K. Kitazaki, N. Miyashita, and N. Koguchi. Tire Deformation Calculating Method And Tire Deformation Calculating Apparatus. US7370523 B2, 2007.
15. Stack TPMS. www.stackltd.com/tpms.html [retrieved 1 May 2014]
16. G. Manla, N. M. White, and J. Tudor. Harvesting Energy From Vehicle Wheels. *Solid-State Sensors, Actuators and Microsystems*, 2009.
17. G. Manla, N. M. White, and M. J. Tudor. Numerical Model Of A Non-Contact Piezoelectric Energy Harvester For Rotating Objects. *Sensors Journal, IEEE*, 2012.
18. L. Gu and C. Livermore. Compact Passively Self-Tuning Energy Harvesting For Rotating Applications. *Smart Materials and Structures*, 2012.
19. F. Khameneifar, M. Moallem, and S. Arzanpour. Modeling and Analysis of a Piezoelectric Energy Scavenger for Rotary Motion Applications. *Journal of Vibration and Acoustics*, 2011.

20. Y. J. Wang, C. D. Chen, C. K. Sung and C. Li. Natural frequency self-tuning energy harvester using a circular Halbach array magnetic disk. *Journal of Intelligent Material System and Structures*, 2012.
21. Y. J. Wang, C. D. Chen, and C. K. Sung. Design of a frequency adjusting device for harvesting energy from a rotating wheel. *Sensors and Actuators A: Physical*, 2010.
22. Y. J. Wang, C. D. Chen, and C. K. Sung. System design of a weighted pendulum type electromagnetic generator for harvesting energy from a rotating wheel. *Mechatronics, IEEE/ASME* , 2012.
23. T. T. Toh, P. D. Mitcheson, A. S. Holmes and E. M. Yeatman. A continuously rotating energy harvester with maximum power point tracking. *Journal of Micromechanics and Microengineering*, 2008.
24. C. Chen, Y. J. Wang, C. Li, S. H. Wang and P. Chang. Swinging Apparatus and Energy Harvester Using The Same. US8166810 B2, 2010.
25. N. Makki and R. Pop-Iliev. Battery and wireless tire pressure measurement system (TPMS) sensor. *Microsystem Technologies*, 2012.
26. N. Makki and R. Pop-Iliev. Piezoelectric power generation for sensor applications: design of a battery-less wireless tire pressure sensor. *SPIE*, 2011.
27. N. Makki and R. Pop-Iliev. Pneumatic tire-based piezoelectric power generation. *in SPIE*, 2011.
28. E. R. Wetsby and E. Halvorsen. Design and Modeling of a Patterned Electret Based Energy Harvester for Tire Pressure Monitoring System. *Mechatronics, IEEE/ASME*, 2011.
29. T. Kvisteroy and N. Hedenstiena. Energy Harvesting System and Method. US20090134632 A1, 2009.

30. J. D. Adamson and G. P. O'brien. System and method for generating electric power from a rotating tire's mechanical energy using piezoelectric fiber composites. US6807853 B2, 2004.
31. N. Ciblak and N. Topaloglu. A Batteryless TPMS Mechanism Concept. Personal Communications, September 2013.
32. M. H. Wu and W. Y. Hsu. Modeling the static and dynamic behavior of a conical spring by considering the coil close and damping effects. *Journal of Sound and Vibration*, 1998.
33. MITCalc <http://www.mitcalc.com/doc/springs/help/en/springs.htm> [retrieved 1 June 2015]
34. R. G. Budynas and J. K. Nisbett, *Shigley's Mechanical Engineering Design*, McGraw Hill, 2013.
35. E. Klarreich. THE SCIENCES Playing Both Sides
<http://www.eleceng.adelaide.edu.au/Groups/parrondo/articles/Playing%20both%20sides,%20Erica%20Klarreich.htm> [retrieved 1 June 2015]
36. ADCATS. PRO-E Analyzer.
http://adcats.et.byu.edu/WWW/ADCATS/Example_Problems/ProE_Analyzer/5Clutch/5Clutch.html [retrieved 1 June 2015]
37. Wikipedia. “Effective mass (spring–mass system)”,
[https://en.wikipedia.org/wiki/Effective_mass_\(spring%E2%80%93mass_system\)#Ideal_uniform_spring](https://en.wikipedia.org/wiki/Effective_mass_(spring%E2%80%93mass_system)#Ideal_uniform_spring) [retrieved 1 June 2015]

APPENDIX A: CONTACT AND COLLISION PROBLEM SIMULATION

Algorithm A.1. Main function

```

%% main code file
clc
close all
clear variables

numCor=1e-6;
%% Parameters
%assembly
H=0.1;
Lr=0.07;
initComp=0.0;

%particle
mc=0.1;%kg
bc=0.005;%N*s/m
kc=100;%N*m

%pulley
Ip=1;%kg*m^2
bp=0.005;%N*m*s/rad
kp=524.88;%N*m/rad
rp=0.008;%m

%generator
Ig=0.001;
bg=4.88e-6;
kb=0.0253;%torque constant
kt=kb;
R=22.9;%ohm
L=13.73e-3 ;

%% Coefficient of Restitutions
eb=0.5;%base

%% Base Parameters
pts=100;
amp=0.02;
Ncycles=5;
freq=5;

```

```

[x,t,deltaT,n]=setTireMotion(pts,amp,Ncycles,freq);

figure
plot(t,x(:,1))
title('Base Motion Position')

%% Initial Positions

[thts,ys,Ts,Ns,offset]=TpmsAssembly(H,Lr,rp,kc,kp,initComp);

x(:,1)=x(:,1)+offset;
y(1,:)=[ys,0,0];
tht(1,:)=[thts,0,0];
alpha(1,:)=[0,0,0];
i(1,:)=[0,0];
power(1)=0;

T(1)=Ts;
N(1)=Ns;
M(1)=0;

%% LOOP
for ii=1:n-1
    %% Boundary Conditions
    %no penetration boundary for base
    if x(ii,1)>y(ii,1)
        y(ii,1)=x(ii,1);
    end
    %rope cannot break boundary
    if thts-tht(ii,1)>(y(ii,1)-ys)*rp
        tht(ii,1)=-(y(ii,1)-ys)*rp+thts;
    end

    %% Collision Calculations
    %collision on base(consevertaion of momentum
    %and energy with coefficient of restitution)
    if x(ii,1)>=y(ii,1) && x(ii,2)-y(ii,2)>0
        y(ii,2)=-eb*(y(ii,2)-x(ii,2))+x(ii,2);
    end
    %collision on pulley(conservation of momentum and energy
    %fully elastic collision
    if thts-tht(ii,1)>=(y(ii,1)-ys)*rp &&
y(ii,2)*rp+tht(ii,2)<0
        k=mc*rp^2/Ip;
        thtb=tht(ii,:);%theta before collision
        tht(ii,2)=(1-k)/(k+1)*tht(ii,2)-
2*k/(rp*(k+1))*y(ii,2);
        y(ii,2)=(k-1)/(k+1)*y(ii,2)-2*rp/(k+1)*thtb(2);

```

```

end
%ratchet engagement
if tht(ii,2)>=alpha(ii,2) && tht(ii,3)-alpha(ii,3)>0
    alpha(ii,3)=tht(ii,3);
end
    %pulley velocity cannot pass generator velocity
if tht(ii,2)>alpha(ii,2)
    alpha(ii,2)=tht(ii,2);
end

%% Force Calculations
%moment
if tht(ii,2)-alpha(ii,2)<-numCor
    M(ii)=0;
else
    M(ii)=Ig*alpha(ii,3)+bg*alpha(ii,2)+kt*i(ii,1);
end
%tension
if thts-tht(ii,1)-(y(ii,1)-ys)*rp<-numCor
    T(ii)=0;
else
T(ii)=(tht(ii,3)*Ip+tht(ii,2)*bp+tht(ii,1)*kp+M(ii))/rp;
end
%normal force
if x(ii,1)-y(ii,1)<-numCor
    N(ii)=0;
else
    N(ii)=y(ii,3)*mc+y(ii,2)*bc+y(ii,1)*kc-T(ii);
end
    %% Motion Calculations
    %conical spring

[y(ii+1,1),y(ii+1,2),y(ii+1,3)]=Solver(mc,bc,kc,N(ii)+T(ii),y
(ii,1),y(ii,2),deltaT);
    %pulley

[tht(ii+1,1),tht(ii+1,2),tht(ii+1,3)]=Solver(Ip,bp,kp,T(ii)*r
p-M(ii),tht(ii,1),tht(ii,2),deltaT);
    %generator

[alpha(ii+1,3),alpha(ii+1,2),alpha(ii+1,1),i(ii+1,3),i(ii+1,2
),i(ii+1,1),power(ii+1)]=GeneratorModule2...
(L,Ig,bg,R,kb,M(ii),i(ii,1),i(ii,2),deltaT);

end

%% Plot Results
%results for conical spring
subplot(5,1,1)

```



```

plot(t,x(:,1))
hold on
plot(t,y(:,1),'r')
SprStatic(1:n)=ys;
plot(t,SprStatic,'k')
title('base motion(blue) Srping(red)')
%results for pulley
subplot(5,1,2)
plot(t,tht(:,1),'r')
title('theta')
hold on
PulStatic(1:n)=thts;
plot(t,PulStatic,'k')
%results for ratchet
subplot(5,1,3)
plot(t,alpha(:,2));
title('generator')
%current results
subplot(5,1,4)
plot(t,i(:,1));
title('current')
%force results
subplot(5,1,5)
plot(t(1:n-1),T);
hold on
% plot(N,'ro')
plot(t(1:n-1),M,'k+')

figure;
plot(t,power)
title('power')

work=t*power';

fprintf('max Normal Force is %f \n',max(N))
fprintf('max Tension is %f \n',max(T))
fprintf('max Ratchet moment is %f \n',max(M))

```

Algorithm A.2. setTireMotion.m function

```

function [x,t,deltT,nn]=setTireMotion(pts,amp,Ncycles,freq)

Tstart=0;

[~,deltT,TPeriod,xPos,xVel,xAcc]=tireMotionCYK(freq,pts,amp);

xdum=[xPos,xVel,xAcc];
x=xdum;

```

```

for ii=1:Ncycles-1
    x=[x;xdum];
end

t=linspace(Tstart,TPeriod*Ncycles,length(x));
nn=length(x);
end

```

Algorithm A.3. tireMotionCYK.m function

```

function [nn,deltaT,TPeriod,x,v,a]=tireMotionCYK(freq,nBump,Y)

bumpR=30/360;%bump ratio in angles

%%
%set time
TPeriod=1/freq;
Tbump=bumpR*TPeriod;%Duration of bump in seconds
t=linspace(0,Tbump,nBump);%time during bump
tRise=t(1:nBump/4);%rise time
TT=tRise(nBump/4);%peak time
deltaT=t(2);

%%
nn=round(TPeriod/deltaT);
x=zeros(nn,1);
v=zeros(nn,1);
a=zeros(nn,1);

%%
%equations giving the motion of bump
amax=120*Y/TT^2;
x(1:nBump/4)=amax/120/TT^3*tRise.^3.*(6*tRise.^2-
15*TT*tRise+10*TT^2);
x(nBump/4+1:3*nBump/4)=x(nBump/4);
x(3*nBump/4+1:nBump)=flipud(x(1:nBump/4));

v(1:nBump/4)=amax/4/TT^3*tRise.^2.*(tRise-TT).^2;
v(nBump/4+1:3*nBump/4)=v(nBump/4);
v(3*nBump/4+1:nBump)=flipud(v(1:nBump/4));

a(1:nBump/4)=amax/TT^3*tRise.*(tRise-TT/2).*(tRise-TT);
a(nBump/4+1:3*nBump/4)=a(nBump/4);
a(3*nBump/4+1:nBump)=flipud(a(1:nBump/4));
end

```

Algorithm A.4. TpmsAssembly.m function

```

function
[thtf,yf,Tf,Nf,offset]=TpmsAssembly(H,Lr,Rp,kc,kt,initComp)

if Lr>H+pi*Rp
    display('rope slack: do not begin')
end

%% assembly of pulley and conical spring
L=(H+pi*Rp-Lr)/(kt+Rp^2*kc);

thts=Rp*kc*L;
ys=kt*L;
Ts=kt/Rp*thts;

%% assembly to the ground

offset=ys+initComp;

thtf=thts-initComp/Rp;
if thtf<=0
    thtf=0;
end
yf=ys+initComp;
Tf=thtf*kt/Rp;
Nf=kc*yf-Tf;

if thtf<0
    display('Error thts<0')
end

end

```

Algorithm A.5. Solver.m function

```

function [x,dx,ddx]=Solver(m,b,k,F,x0,dx0,t)
%this function solves second order linear differential
equations
%where m(mass)=kg b(damping)=N*s/m k(spring constant)=N/m

if(k==0 && b~=0)
    %solve for k=0 and b!=0
    C2=m/b*(F/b-dx0);
    C1=x0-C2;
    x=F/b*t+C2*exp(-b/m*t)+C1;
    dx=F/b-b/m*C2*exp(-b/m*t);

```

```

    ddx=(b/m)^2*C2*exp(-b/m*t);
end

if(b==0 && k~=0)
    %solve for k!=0 and b=0
    wn=sqrt(k/m);
    A=dx0/wn;
    B=x0-F/k;
    x=F/k+A*sin(wn*t)+B*cos(wn*t);
    dx=A*wn*cos(wn*t)-B*wn*sin(wn*t);
    ddx=-A*wn^2*sin(wn*t)-B*wn^2*cos(wn*t);
end

if(b==0 && k==0)
    %solve for k=0 and b=0
    C2=x0;
    C1=dx0;
    x=1/2*F/m*t^2+C1*t+C2;
    dx=F/m*t+C1;
    ddx=F/m;
end

if(k~=0 && b~=0)
    f=F/m;
    wn=sqrt(k/m);
    zeta=b/(2*m*wn);
    if zeta<1
        %solve for underdamped system
        wd=wn*sqrt(1-zeta^2);
        wd=wn*sqrt(1-zeta^2);
        B=x0-F/k;
        A=(dx0+zeta*wn*B)/wd;
        x=F/k+exp(-zeta*wn*t)*(A*sin(wd*t)+B*cos(wd*t));
        dx=exp(-zeta*wn*t)*(-(zeta*wn*A+wd*B)*sin(wd*t)+(A*wd-
zeta*wn*B)*cos(wd*t));
    end

    if zeta==1
        %solve for critically damped system
        B=x0-F/m;
        A=dx0+wn*B;
        x=F/k+(A*t+B)*exp(-wn*t);
        dx=(-wn*A*t+A-wn*B)*exp(-wn*t);
    end

    if zeta>1
        %solve for overdamped system
        wd=wn*sqrt(zeta^2-1);
        B=(dx0+(wd+zeta*wn)*(x0-F/k))/(2*wd);
        A=x0-F/k-B;
        x=F/k+exp(-zeta*wn*t)*(A*exp(-wd*t)+B*exp(wd*t));
    end
end

```

```

dx=A*(-wd-zeta*wn)*exp((-wd-zeta*wn)*t)+B*(wd-
zeta*wn)*exp((wd-zeta*wn)*t);
end
ddx=f-2*zeta*wn*dx-wn^2*x;
end
end

```

Algorithm A.6. GeneratorModule2.m function

```

function
[ddalpha,dalpha,alpha,ddi,di,i,power]=GeneratorModule2...
(L,I,b,R,kb,Mr,i0,di0,t)
% L;%indctance
% I;%inertia
% b;%damping
% R;%resistance
% kb;%electrical constant
kt=kb;
% Mr;%applied moment

m=L*I;
c=L*b+R*I;
k=kb*kt+R*b;
f=kb*Mr;

[i,di,ddi]=Solver(m,c,k,f,i0,di0,t);

%% Solve for motion
alpha=0;
dalpha=(L*di+R*i)/kb;
ddalpha=L/kb*ddi+R/kb*di;

power=i*R^2;
end

```

APPENDIX B: COMPLETE POWER TRANSMISSION TO PULLEY

Algorithm B.1. Main function

```

clc
clear variables
close all

ncyc=3;%number of cycles
nn=1000;%number of data points

load=10;
%pulley properties
Rp=8e-3;%pulley radius m

period=0.89;
angvel=2*pi/period; %rad/s
Vms=angvel*0.2; %m/s
%% Create n cycles of tire motion
[x,t,dt]=TireMotionV(Vms,nn,ncyc);

figure
subplot(3,1,1)
plot(t,x(:,1))
title('tire position')

subplot(3,1,2)
plot(t,x(:,2))
title('tire velocity')

subplot(3,1,3)
plot(t,x(:,3))
title('tire acceleration')

%% Pulley motion

theta=-x/Rp;

% plot(theta(:,1))

%% Initial Values
alpha=[0 0];
i=[0 0];
M=[0];

```

```

power=[0];

%% Simulate motion using dt time intervals

for ii=1:(nn*ncyc)-1

    %engagement check
    if theta(ii,2)>alpha(ii,1)
        RE=1;
    end
    if theta(ii,2)<=0 || (theta(ii,2)>0 &&
theta(ii,3)<alpha(ii,2))
        RE=0;
    end
    [dummyi,dummyalpha,dummyM,power(ii+1)]=...

generatorDyn3(theta(ii,:),alpha(ii,:),i(ii,:),RE,dt,load);
    alpha=[alpha;dummyalpha];
    i=[i;dummyi];
    M=[M,dummyM];
end

%% Calculate RMS power
RMSPOW= sqrt(sum((i(:,1).^2*load).^2)/(nn*ncyc));
fprintf('RMS POWER IS %f Watt\n',RMSPOW)

%% Plot results
figure
subplot(5,1,1)
plot(t,theta(:,2),'r')
hold on
plot(t,alpha(:,1))
title('motor velocity blue pulley red')

subplot(5,1,2)
plot(t,theta(:,3),'r')
hold on
plot(t,alpha(:,2))
title('motor acceleration blue pulley red')

subplot(5,1,3)
plot(t,i(:,1))
title('current')

subplot(5,1,4)
plot(t,M)
title('Ratchet moment')

subplot(5,1,5)

```

```
plot(t,power)
title('Power')
```

Algorithm B.2. TireMotionV.m function

```
function [x,t,dt]=TireMotionV(V,nn,ncyc)
%V in m/s
n=10000;
R=200e-3;%radius in m
h=20e-3;%height in m

beta=acos((R-h)/R);%degrees
omega=V/R;%rad/s

Tpeak=beta/omega;%s
Ttot=2*pi/omega;

TTrise=linspace(0,Tpeak,n);
delt=TTrise(2)-TTrise(1);

TTdown=linspace(TTrise(n)+delt,2*Tpeak,n-1);

TTrest=linspace(TTdown(n-1)+delt,Ttot,n-1);

% TTrest=linspace(TTdown(n),Ttot,n/2);

%rise
ralpha=omega*TTrise;
xr=R-(R-h)./cos(beta-ralpha);

%down
dalphi=omega*TTdown;
xd=R-(R-h)./cos(beta-dalphi);

%rest
xrest=R-R*ones(1,n-1);

pos=[xr,xd,xrest];
TT=[TTrise,TTdown,TTrest];

% figure
% plot(TT,x)

up=spline(TT,pos);%position
vp=fnder(up,1);%velocity
ap=fnder(up,2);%acceleration

time=linspace(0,Ttot,nn);
```



```

dt=time(2)-time(1);

u=ppval(up,time);
v=ppval(vp,time);
a=ppval(ap,time);
u=u';
v=v';
a=a';

d=[];
dd=[];
ddd=[];
for ii=1:1:ncyc
    d=[d;u];
    dd=[dd;v];
    ddd=[ddd;a];
end

t=[];
tdummy=0;
for ii=1:1:ncyc
    t=[t time+tdummy];
    tdummy=t(nn*ii);
end
x=[d dd ddd];

% figure
% subplot(3,1,1)
% plot(t,x(:,1))
% subplot(3,1,2)
% plot(t,x(:,2))
% subplot(3,1,3)
% plot(t,x(:,3))

end

```

Algorithm B.2. generatorDyn3.m function

```

function
[i,alpha,M,power]=generatorDyn3(theta,alpha0,i0,RE,dt,load,ex
tload)

%generator properties
I=8.3e-7;%inertia kg m^2
b=1.39e-6;%damping N m s/rad
L=13.73e-3;%inductance H
k=0.0139;%electrical constant V s/rad
R=22.9+load+extload;%total resistance ohm

```

```

brat=6e-4;%ratchet damping N-m-s/rad
%Ratchet engaged case
if RE==1
    alpha(1,1:2)=theta(1,2:3);
    %   alpha(1,1)=theta(1,2);
    %   if alpha0(1,2)<theta(1,3)
    %       alpha(1,2)=theta(1,3);
    %   else
    %       alpha(1,2)=alpha0(1,2);
    %   end

    i(1,1)=k*alpha(1)/R+(i0(1)-k*alpha(1)/R)*exp(-R/L*dt);
    i(1,2)=k/L*alpha(1)-R/L*i(1,1);
    M=(I*alpha(1,2)+b*alpha(1,1)+k*i(1,1));
    if M<0
        display('check for error')
    end
%ratceht disengaged case
else
    %   if alpha0(1)<=0
    %       M=0;
    %   else
    %       M=-Mrat;
    %   end
    M=0;
    beff=b+brat;
    %   m=L*I;
    %   c=L*beff+R*I;
    %   z=k^2+R*beff;
    %   f=R*M;
    %   [alpha(1,1),alpha(1,2),dddalpha]=...
    %       Solver(m,c,z,f,alpha0(1),alpha0(2),dt);
    %   i(1,1)=(-I*alpha(1,2)-beff*alpha(1,1))/k;
    %   i(1,2)=(-I*dddalpha-beff*alpha(1,2))/k;
    A=[-beff/I,-k/I;k/L,-R/L];
    s0=[alpha0(1);i0(1)];
    s=expm(A*dt)*s0;
    sdot=A*s;
    alpha=[s(1),sdot(1)];
    i=[s(2),sdot(2)];
end

power=i(1,1)^2*load;
end

```